The rôle of the complete Coriolis force in cross-equatorial flow of abyssal ocean currents

A. L. Stewart and P. J. Dellar

OCIAM, Mathematical Institute, 24-29 St Giles', Oxford, OX1 3LB, UK

Abstract

Ocean currents flowing close to or across the equator are strongly constrained by the change in sign of f, the locally vertical component of the Earth's rotation vector, across the equator. We investigate these currents using a shallow water model that includes both the locally vertical and locally horizontal components of the Earth's rotation vector, thus accounting for the complete Coriolis force. We therefore avoid making the so-called "traditional approximation" that retains only the part of the Coriolis force associated with the locally vertical component of the rotation vector. Including the complete Coriolis force contributes an additional term to the fluid's potential vorticity, which may partially balance the change in sign of f as fluid crosses the equator over suitably shaped bathymetry.

We focus on the Antarctic Bottom Water, which crosses the equator northwards in the western Atlantic ocean where the local bathymetry forms an almost-zonal channel. We show that this bathymetry facilitates the current's equatorial crossing via the action of the "non-traditional" component of the Coriolis force. We illustrate this process using both analytical and numerical solutions for flow of an abyssal current over idealised equatorial topography. We also consider the one-dimensional geostrophic adjustment of a body of fluid across the equator, and show that the "non-traditional" contribution to the fluid's angular momentum permits a larger cross-equatorial transport. These results underline the importance of including the complete Coriolis force in studies of the equatorial ocean, particularly in the weakly-stratified abyssal ocean where the non-traditional component is most pronounced.

Keywords:
Antarctic Bottom Water, interhemispheric flow, equatorial currents, traditional approximation, complete Coriolis force

1. Introduction

This paper is concerned with an aspect of equatorial ocean dynamics that has received little attention in connection with abyssal currents — the complete Coriolis force. The component of the Coriolis force associated with the locally horizontal component of the Earth's rotation vector is almost universally neglected. This approximation was named the traditional approximation by Eckart (1960), as it was originally introduced for convenience in studies of linear waves in stratified fluids. It has later been justified using various scaling arguments. Gerkema et al. (2008) have recently reviewed the rôles of the traditional approximation and the complete Coriolis force, but to the best of our knowledge there have been no previous studies of the complete Coriolis force in the context of abyssal ocean currents.

We base our study on the Antarctic Bottom Water (AABW) due to its unusual behaviour close to the equator. The AABW originates from ice melting in the Weddell Sea on the coast of Antarctica, and flows north through the Atlantic as a deep western boundary current, until it reaches the equator. Much of the current then turns east, in agreement with the classical geostrophic theory of Stommel and Arons (1960), but a substantial portion continues northwest through the Cera Abyssal Plain, where it has been observed as far as 11°N (Friedrichs and Hall, 1993). A series of observations in the 1990s (Hall et al., 1994, 1997; Rhein et al., 1998), conclude that, of approximately 5 Sv (1 Sv = $10^6\,\mathrm{m}^3\,\mathrm{s}^{-1}$) approaching the equator, around 2 Sv crosses into the northern hemisphere.

In Fig. 1 we plot the large-scale features of the bathymetry in the relevant area close to the equator. The AABW enters this region from the south as a western boundary current, but much of it turns eastward before it reaches the equator. However, around 2 Sv passes through the almost-westward channel in the centre of the figure, and through to the northern hemisphere. Our study shows that the structure and orientation of this channel is important for cross-equatorial transport of the AABW, particularly in the context of the complete Coriolis force.

Cross-equatorial flow is inhibited by the change in the sign of f, the locally vertical component of the Earth's rotation vector, across the equator. To conserve potential vorticity, the flow must acquire relative vorticity, and this limits the extent to which it can penetrate into the northern hemisphere. Edwards and Pedlosky (1998) discuss this process in detail, and conclude that modification of the potential vorticity via dissipation is required to permit the flow observed in currents like the AABW.

A series of studies have attempted to explain cross-equatorial flow using shallow water models. Nof and Olson (1993) showed that the frontal blocking constraint for a northward-flowing western boundary current (Nof, 1990) is completely relaxed when an opposing channel wall is introduced. Nof and Borisov (1998) later conducted some numerical simulations in an idealised channel, and showed that flow across the equa-

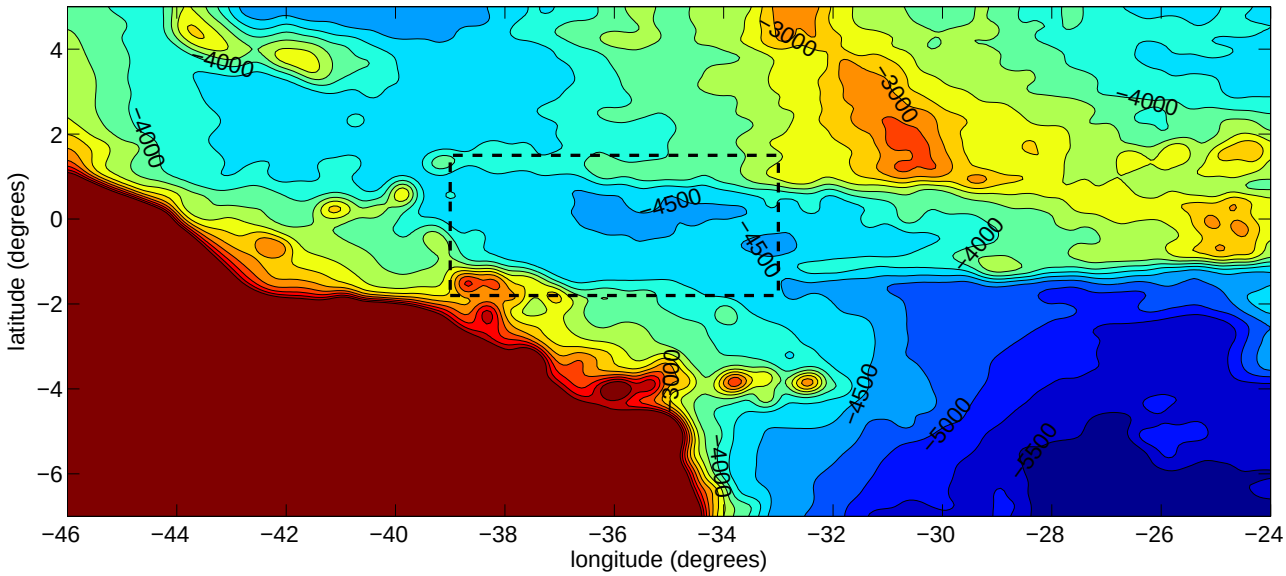

Figure 1: Contours of the bathymetry in the region where the AABW crosses the equator, shaded at intervals of 250 m. The data has been taken from Amante and Eakins (2009), and smoothed via six applications of a nine-gridpoint average (c.f Choboter and Swaters, 2004) to remove small-scale features. A longitudinally averaged profile view of the area within the dashed rectangle is shown in Fig. 3(a).

tor was dominated by inertial effects and the channel geometry. Stephens and Marshall (2000) performed numerical integrations of the frictional-geostrophic shallow water equations to model the path of the AABW through realistic bathymetry over almost the entire Atlantic ocean. In particular, they found a realistic cross-equatorial transport of AABW in the western Atlantic. Choboter and Swaters (2000) evaluated the frictional-geostrophic model in the context of abyssal currents, and found that it accurately captured certain aspects of the full shallow water equations. However, a later study by Choboter and Swaters (2004) of the AABW with full bathymetry showed that it was difficult to describe cross-equatorial flow accurately within the limitations of a frictional-geostophic model.

None of these papers consider the influence of the complete Coriolis force on cross-equatorial flow. Moving away from shallow water theory, a theoretical study of flow in a spherical annulus by Schopp and Colin de Verdière (1997) showed that fluid could cross the equatorial plane in Taylor columns aligned with the rotation axis (which is locally horizontal at the equator). Raymond (2000) studied large-scale atmospheric cross-equatorial flows using a linear two-dimensional solution of the continuously-stratified fluid equations, and found a class of oscillations that depend entirely on the non-traditional component of the Coriolis force. Dellar and Salmon (2005) and Stewart and Dellar (2010) have since shown how the complete Coriolis force may be included in shallow water theory, as discussed briefly in Section 2. By solving these equations in certain idealised scenarios, we show that the "non-traditional" effects associated with the complete Coriolis force may substantially influence the behaviour of an abyssal current as it crosses the equator.

The structure of this paper is as follows. In Section 2, we discuss the inclusion of the complete Coriolis force in the shallow water equations. In Section 3, we discuss the modification of the potential vorticity by the complete Coriolis force, and describe the influence that this should have on the AABW. In Sections 4 and 5, we consider steady and unsteady solutions for the flow of an abyssal current in a zonally uniform channel. This illustrates how the action of the non-traditional component of the Coriolis force in a zonal channel may facilitate the equatorial crossing of the AABW. In Section 6, we revisit the one-dimensional cross-equatorial geostrophic adjustment problem of Killworth (1991), and show that the action of the complete Coriolis force on the current's angular momentum allows more fluid to adjust further across the equator. Finally, in Section 7 we discuss our results, their implications, and the outlook for future work in this area.

2. Shallow water equations on a non-traditional β-plane

Shallow water theory underlies all of the analysis in this work. The standard shallow water equations offer a useful conceptual model of an abyssal current, as used previously for analytical (Nof and Olson, 1993) and numerical (Choboter and Swaters, 2004) studies of the AABW. In this work we use the extended shallow water equations that include the complete Coriolis force (Dellar and Salmon, 2005; Stewart and Dellar, 2010; Dellar, 2011).

Our starting point is the three-dimensional Euler equations for an incompressible fluid on a non-traditional equatorial β-

plane,

$$\frac{\mathrm{D}u}{\mathrm{D}t} - 2\Omega_z v + 2\Omega_y w + \frac{1}{\rho}\frac{\partial p}{\partial x} = 0, \tag{1a}$$

$$\frac{\mathrm{D}v}{\mathrm{D}t} + 2\Omega_z u + \frac{1}{\rho}\frac{\partial p}{\partial y} = 0, \tag{1b}$$

$$\frac{\mathrm{D}w}{\mathrm{D}t} - 2\Omega_y u + \frac{1}{\rho}\frac{\partial p}{\partial z} + g = 0, \tag{1c}$$

$$\frac{\partial u}{\partial x} + \frac{\partial v}{\partial y} + \frac{\partial w}{\partial z} = 0. \tag{1d}$$

These equations are formulated in a set of pseudo-Cartesian curvilinear coordinates with x directed eastward, y northward, and z vertically upwards. The x and y coordinates define curved surfaces of constant geopotential, so the combination of the gravitational and centrifugal accelerations appears only through the g term in the vertical momentum equation. The geometrical difficulties that arise in the derivation of the mid-latitude β-plane approximation (*e.g.* Veronis, 1963, 1981; Phillips, 1973; Dellar, 2011) are greatly reduced for the equatorial β-plane approximation.

The components of the three-dimensional velocity are u, v, and w, p is the fluid pressure, ρ is the constant density, and $D/Dt = \partial_t + u\partial_x + v\partial_y + w\partial_z$ is the material time derivative. The Coriolis parameters are $\Omega_y = \Omega$ (constant) and $\Omega_z = \beta y$ with $\beta = 2\Omega/R_E$, where Ω is the Earth's rotation frequency and R_E the Earth's radius. The latitude coordinate may be taken to be $y = R_E \sin\phi$, where ϕ is latitude. Equations (1) are the equatorial form of the non-traditional β-plane equations derived by Grimshaw (1975) using Mercator coordinates.

For our purposes it is sufficient to use the quasihydrostatic form of these equations that omits the Dw/Dt term in (1c). The quasihydrostatic approximation was introduced by White and Bromley (1995) as a less severe form of the widely used hydrostatic approximation that omits both the Dw/Dt and the $-2\Omega_y u$ terms from the vertical momentum equation. The quasihydrostatic form of (1a)–(1d) may be derived from the Euler equations for flow on a rotating sphere under the following assumptions:

(i) the ratio of vertical to horizontal length scales is small (the *shallow water* approximation), $\alpha = \mathcal{H}/\mathcal{L} \ll 1$;

(ii) the ratio of the horizontal length scale to the Earth radius is small, $\varepsilon = \mathcal{L}/R_E \ll 1$;

where $\mathcal{U}$ is a horizontal velocity scale. Dellar (2011) derived (1a)–(1d) by approximating the Lagrangian for the three-dimensional Euler equations in spherical geometry using assumptions (i) and (ii) in the distinguished limit

$$\alpha \sim \varepsilon \ll 1. \tag{2}$$

The familiar conservation laws for energy, angular momentum, and potential vorticity in spherical geometry may be derived from symmetries of a Lagrangian via Noether's theorem that relates symmetries to conservation laws. Conservation of energy arises from a translation symmetry in time, and conservation of zonal angular momentum arises from a rotational symmetry about the Earth's axis. Material conservation of potential vorticity arises from a more subtle particle relabelling symmetry (Ripa, 1981; Salmon, 1982). Dellar's (2011) derivation of the quasihydrostatic equations on an equatorial β-plane preserves all these symmetries in the approximated Lagrangian, so the resulting equations inherit exact conservation laws for energy, angular momentum, and potential vorticity. Grimshaw (1975) previously gave a direct proof of potential vorticity conservation on the non-traditional β-plane by manipulating (1a)–(1d).

Multi-layer shallow water theory describes the behaviour of a number of superposed layers of fluid of thickness $h_i(x, y, t)$, for $i = 1, \ldots, N$, overlying an arbitrary bottom topography $z = h_b(x, y)$. Throughout this work we refer to the actual measured height of the ocean bed as 'bathymetry', and to the model ocean bed as 'topography'. This is represented schematically in Fig. 2.

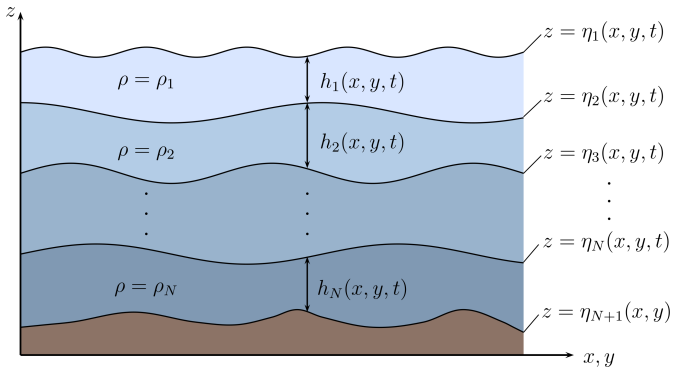

Figure 2: A schematic of the multi-layer shallow water model.

Stewart and Dellar (2010) derive the multi-layer shallow water equations from (1a)–(1d) by making the further assumption of columnar motion in the three-dimensional Lagrangian, following Miles and Salmon's (1985) derivation of the Green and Naghdi (1976) equations, and Dellar and Salmon's (2005) derivation of the single layer shallow water equations with the complete Coriolis force. Being derived from a Lagrangian, the resulting shallow water equations also possess exact conservation laws for energy, angular momentum, and potential vorticity. For example, the potential vorticity conservation law for a single layer is given by equation (6) in §3 of this paper.

We denote the depth-averaged horizontal fluid velocity in each layer as $\mathbf{u}_i(x, y, t) = (u_i(x, y, t), v_i(x, y, t))$ for $i = 1, \ldots, N$, and the density of each layer by ρ_i. The position of the upper surface of each layer is $z = \eta_i(x, y, t)$, where $z = \eta_1(x, y, t)$ corresponds to the free surface of the fluid, and $z = \eta_{N+1}(x, y) = h_b(x, y)$ corresponds to the bottom topography. Following Stewart and Dellar (2010) and Dellar (2011), the multi-layer shallow water equations on the non-traditional equatorial β-plane may

be written as

$$\frac{\mathrm{D}_i\mathbf{u}_i}{\mathrm{D}t} + \left(\beta y - \Omega\frac{\partial}{\partial y}\left(\eta_i + \eta_{i+1}\right)\right)\hat{\mathbf{z}}\times\mathbf{u}_i + \Omega\frac{\partial}{\partial t}\left(\eta_i + \eta_{i+1}\right)\hat{\mathbf{x}} + \nabla\left(g\,\eta_i - \Omega h_i u_i + \frac{1}{\rho_i}\sum_{j=1}^{i-1}\rho_j h_j (g - 2\,\Omega u_j)\right) = 0, \tag{3}$$

$$\frac{\partial h_i}{\partial t} + \nabla\cdot(h_i\mathbf{u}_i) = 0. \tag{4}$$

The advective derivative is written $\mathrm{D}_i/\mathrm{D}t \equiv \partial/\partial t + \mathbf{u}_i\cdot\nabla$, where $\nabla \equiv (\partial/\partial x, \partial/\partial y)$. We write $\hat{\mathbf{x}}$ and $\hat{\mathbf{z}}$ for the unit vectors in the x and z directions respectively. The non-traditional contributions to the pressure gradient arise due to the change from hydrostatic to quasihydrostatic balance (White and Bromley, 1995) through the retention of the $-2\Omega_y u$ term in the vertical momentum equation (1c). The other terms modify the fluid's angular momentum to reflect the fact that changes in the layer depth correspond to changes in the fluid's perpendicular distance from the axis of rotation, analogous to the $2\Omega_y w_i$ term in (1a).

The existence of exact conservation laws for angular momentum and potential vorticity might appear at odds with the statements found in White and Bromley (1995) and Marshall et al. (1997) that including the complete Coriolis force while making the shallow atmosphere approximation together preclude conservation laws for angular momentum and potential vorticity. However, it is important to distinguish between the *shallow water* approximation, given by condition (i) above, and the *shallow atmosphere* approximation, associated with the complete neglect of terms involving the ratio of the vertical lengthscale to the planetary radius. For example, the shallow atmosphere approximation is commonly taken to imply the replacement of true spherical radius r by the constant Earth's radius R_E in the Euler equations formulated in spherical polar coordinates.

We use the name "shallow water" to reflect the status of (3) and (4) as depth-averaged equations derived under the approximation (i). However, the shallow water momentum equation retains various terms proportional to Ωh_i and $\Omega\eta_i$ that are formally $O(\alpha)$ smaller than the other terms, just as the Green and Naghdi (1976) equations retains small terms of $O(\alpha^2)$ arising from the Dw/Dt term in the three-dimensional Euler equations. The retained terms are formally proportional to $\mathcal{H}/R_E$, so our equations are "deep atmosphere" shallow water equations. One justification for retaining these formally small terms is that the leading-order term in the expansion of the relevant part of the Lagrangian is a "null Lagrangian" that does not contribute to the equations of motion (Dellar, 2011).

Equations (3) and (4) describe the motion of fluid columns aligned with the locally vertical axis. Following the Tayor–Proudman theorem, one might expect the columns to be aligned with the axis of rotation, which is perpendicular to the locally vertical axis at the equator. However, motion predominantly in vertical columns is still compatible with the three-dimensional Euler equations under the small aspect ration assumption $\alpha = \mathcal{H}/\mathcal{L} \ll 1$, even when the rotation axis is locally horizontal. Additionally, the real AABW flow is strongly inertial (Nof and Olson, 1993; Nof and Borisov, 1998) slightly stratified, and subject to the action of bottom friction. All these effects will tend to inhibit the fluid from moving in Taylor columns. We thus expect our shallow water model to provide a useful qualitative description of the behaviour of the AABW.

3. The rôle of potential vorticity

The ability of fluid to cross the equator is strongly constrained by conservation of potential vorticity (*e.g.* Killworth, 1991). We shall now examine the mechanisms by which this constraint is imposed, and the influence of the complete Coriolis force upon it.

Let us consider a single layer of fluid governed by the non-traditional shallow water equations, with horizontal velocity $\mathbf{u}(x,y,t) = (u(x,y,t), v(x,y,t))$ and thickness $h(x,y,t)$, overlying topography $z = h_b(x,y)$. The angular momentum conservation law for the layer is (c.f. Ripa, 1982, 1997)

$$\frac{\mathrm{D}\tilde{u}}{\mathrm{D}t} = -\frac{1}{h}\frac{\partial}{\partial x}\left[\tfrac{1}{2}h^2\,(g - 2\Omega u)\right] - (g - 2\Omega u)\frac{\partial h_b}{\partial x}, \tag{5}$$

where $\tilde{u} = u - \frac{1}{2}\beta y^2 + 2\Omega\bar{z}$ is the (zonal) angular momentum and $\bar{z} = h_b + h/2$ is the half-layer height, or equivalently the average vertical position of the fluid in a column. Equation (5) thus equates changes in angular momentum with the torque exerted by zonal pressure gradients. The term proportional to Ω in $\tilde{u}$ as defined in (5) is a non-traditional Coriolis term that accounts for the change in a fluid column's average distance from the rotation axis due to changes in h and h_b.

The quantity $\tilde{u}$ is also the canonical momentum in the Lagrangian formulation, and also appears in the potential vorticity conservation law,

$$\frac{\mathrm{D}q}{\mathrm{D}t} = 0, \quad q = \frac{1}{h}\left(\beta y - 2\Omega\frac{\partial\bar{z}}{\partial y} + \zeta\right) = \frac{\hat{\mathbf{z}}\cdot(\nabla\times\tilde{\mathbf{u}})}{h}, \tag{6}$$

where $\zeta = \partial_x v - \partial_y u$ is the relative vorticity and $\tilde{\mathbf{u}} = (\tilde{u}, v)$. The last term in (6) is the general expression for the conserved potential vorticity in terms of the canonical momenta $\tilde{u}$ and $\tilde{v} = v$, as given by the particle relabelling symmetry. Equation (6) may also be interpreted as the depth average of a three-dimensional Ertel potential vorticity (see Dellar and Salmon, 2005).

Now consider fluid columns moving northwards across the equator under the traditional approximation, equivalent to setting $\Omega = 0$ in (6). The βy term in (6) changes sign as the columns cross the equator, the line $y = 0$, which requires a corresponding change in h and/or ζ to conserve q. Hua et al. (1997) have shown that the fluid will be subject to a symmetric instability if the three-dimensional Ertel potential vorticity Q_E does not have the same sign as y. This suggests that equator-crossing fluid should have $Q_E \approx 0$, which Hua et al. (1997) show is consistent with PEQUOD data for the deep ocean (Firing, 1987). The change in the planetary vorticity βy in each fluid column must thus typically be balanced by a change in the relative vorticity ζ. Killworth (1991) has shown that this necessary generation of relative vorticity severely constrains the penetration of inviscid fluid into the northern hemisphere.

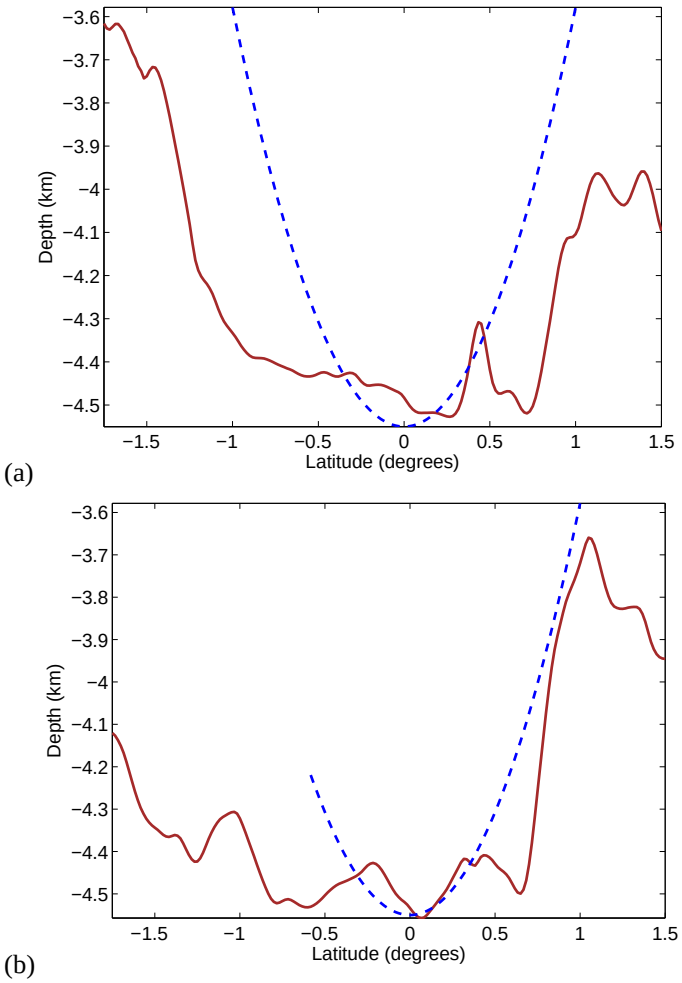

Figure 3: A comparison of the measured bathymetry (data from Amante and Eakins, 2009) in the western equatorial Atlantic with the ideal topography described by (7). The bathymetry has been zonally averaged between (a) 39°W and 34°W, as marked in Fig. 1, and (b) 36°W and 33°W.

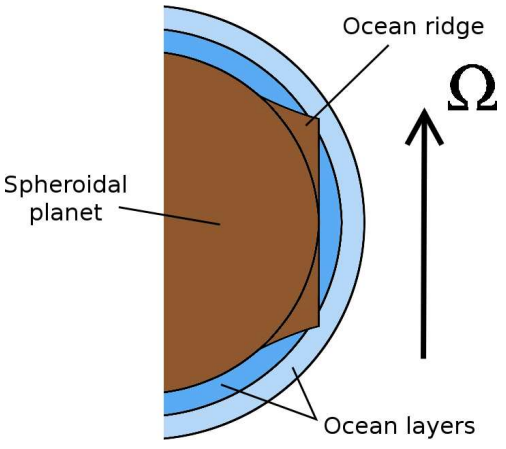

Figure 4: A greatly exaggerated illustration of the conditions under which the fluid would experience no change in planetary vorticity, or equivalently no change in planetary angular momentum, in the region close to the equator. Large submarine ridges form a channel-like equatorial topography, such that fluid moving close to the equator remains at a constant distance from the rotation axis.

Including the complete Coriolis force offers an alternative means of balancing the change in the planetary vorticity βy as fluid crosses the equator. In fact, the βy term is balanced completely by the topography alone if

$$h_b = h_0 + \frac{\beta}{4\Omega} y^2 = h_0 + \frac{1}{2R_E} y^2 \tag{7}$$

where h_0 is a constant reference height. This describes a zonal channel that is symmetric about the equator, a configuration which is particularly relevant for the AABW. In Fig. 3 we compare the zonally-averaged bathymetry in the western equatorial Atlantic ocean with the ideal topography described by (7). We find a good qualitative agreement between the shapes of the channels between 39°W and 34°W, and remarkably good agreement on the northern side of the channel between 36°W and 33°W. As a result, we expect that including the complete Coriolis force should play a particularly important rôle in the equatorial crossing of the AABW. The AABW traverses a zonal channel, so the non-traditional component of the Coriolis force should at least partly balance the change in sign of the traditional component. The fluid should then be able to cross the equator without needing to generate as much relative vorticity.

This process may be understood more intuitively in spherical geometry, though we will retain the equatorial β-plane approximation, $\Omega_y \approx \Omega$ and $\Omega_z \approx \beta y$. The first two terms in the numerator of the potential vorticity (6) may be written as

$$\beta y - 2\Omega \frac{\partial \overline{z}}{\partial y} = 2\boldsymbol{\Omega} \cdot \nabla_3 (z - \overline{z}) = \zeta_p, \tag{8}$$

where $\nabla_3 = (\partial_x, \partial_y, \partial_z)$ is the three-dimensional gradient vector. The right-hand side of (8), which we will refer to as the complete planetary vorticity ζ_p, is the component of the three-dimensional rotation vector $\boldsymbol{\Omega}$ that lies normal to the half-layer height of the fluid at any point (see Dellar and Salmon, 2005). This may also be interpreted as the depth-average of the component normal to surfaces of constant Lagrangian label $c = (z - h_b)/(h - h_b)$. In a layer of constant depth, $h \equiv H$ say, the planetary vorticity is 0 wherever $\boldsymbol{\Omega}$ is parallel to the local topography. Thus, the ideal topography described by (7) corresponds to the equatorial part of the spherical earth being levelled in such a way that the fluid layer lies parallel to the rotation axis, as illustrated in Fig. 4. The condition $\zeta_p \equiv 0$ is equivalent to the condition that the planetary contribution to the angular momentum (5) is everywhere constant, $\tilde{u}_p = 2\Omega\overline{z} - \frac{1}{2}\beta y^2 \equiv$ constant. This provides a more intuitive interpretation of Fig. 4, where the fluid remains at an approximately constant distance from the rotation axis, and so does not require a large change in its relative angular momentum u as it crosses the equator.

The importance of the non-traditional component of the Coriolis force is typically estimated using dimensionless numbers such as the ratio of vertical to horizontal lengthscales, or the ratio of the inertial frequency f to the Brunt–Väisälä frequency N (*e.g.* Gerkema et al., 2008). The ratio f/N determines the ratio of vertical to horizontal lengthscales in the three-dimensional quasigeostrophic regime (*e.g.* Pedlosky, 1987; White, 2002). Another relevant dimensionless number is based on the veloc-

ity scale $2\Omega\mathcal{H}$, which is the change in zonal velocity experienced by a fluid parcel that changes its height by the vertical lengthscale $\mathcal{H}$ while conserving angular momentum (White and Bromley, 1995).

To see how this velocity scale enters our analysis, the magnitude of the non-traditional Coriolis term $-2\Omega\,\partial\bar{z}/\partial y$ relative to the traditional Coriolis term βy may be estimated as

$$\delta = \frac{2\Omega\mathcal{H}}{\beta\mathcal{L}^2} = \frac{\mathcal{H}R_E}{\mathcal{L}^2}, \tag{9}$$

where $\mathcal{L}$ and $\mathcal{H}$ are vertical and horizontal lengthscales respectively. If we naively define $\mathcal{L} = 300$ km and $\mathcal{H} = 500$ m, based on Fig. 3, we obtain $\delta \approx 0.04$. For a more systematic approach we take the horizontal lengthscale $\mathcal{L}$ to be the equatorial deformation radius

$$\mathcal{L} = R_d = \frac{(g'\mathcal{H})^{1/4}}{\beta^{1/2}} \quad \text{so} \quad \delta = 2\Omega\sqrt{\frac{\mathcal{H}}{g'}}, \tag{10}$$

where g' is a reduced gravity (see next section). The second equation may also be interpreted as defining

$$\delta = 2\Omega\mathcal{H}/\sqrt{\mathcal{H}g'} \tag{11}$$

to be the ratio of the non-traditional velocity scale $2\Omega\mathcal{H}$ to the internal wave speed $\sqrt{\mathcal{H}g'}$. Even for weak stratification ($g' \approx 10^{-3}$) we obtain $\delta \approx 0.1$. However, the analysis of this and later sections shows that these scaling arguments underestimate the influence of the non-traditional component of the Coriolis force.

Equation (9) also suggests a characteristic horizontal lengthscale $\mathcal{L} = \sqrt{\mathcal{H}R_E}$ on which non-traditional effects become significant near the equator. This lengthscale was first obtained by Stern (1963) and Bretherton (1964) in their studies of low frequency Poincaré (or gyroscopic) waves that are trapped near the equator, and later by Colin de Verdière and Schopp (1994) in their theory of nonlinear motions near the equator.

4. Steady flow in a zonally-uniform channel

As a first step towards understanding more thoroughly how the complete Coriolis force influences the flow of the AABW, we approximate the bathymetry between 39°W, 34°W, 1.5°S and 1.5°N as a zonally-uniform channel (see Fig. 1). We consider the steady flow of a shallow fluid layer over this topography to illustrate how the complete Coriolis force might influence a current crossing the equator.

4.1. Solution for a single layer

We seek a steady, zonally-symmetric solution of the single-layer shallow water equations equations, representing an abyssal current flowing beneath a deep, quiescent upper layer.

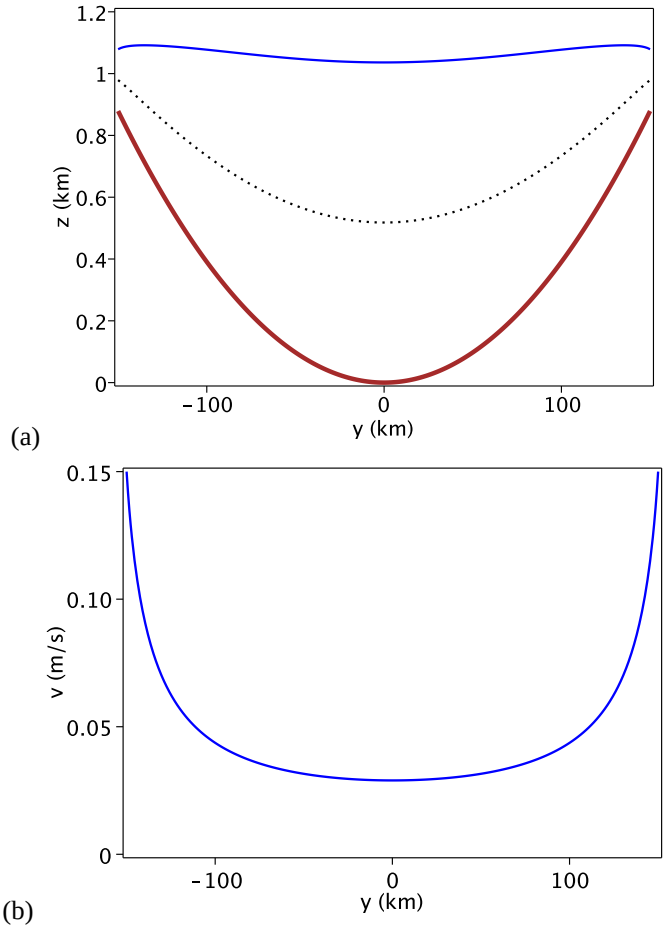

Figure 5: Plots of the solution described by (13)–(15), for the case $y_0 = -150$ km, $U = 0\,\mathrm{m\,s^{-1}}$, $V = 0.15\,\mathrm{m\,s^{-1}}$, $H = 200$ m, and $g' = 5\times10^{-4}\,\mathrm{m^2\,s^{-1}}$. In (a) we show the bottom topography (thick line), the height of the layer above it (thin line), and the half-layer depth (dotted line). In (b) we show the meridional velocity. Both plots include the complete Coriolis force, as there is no perceptible change in these variables when the traditional approximation is made.

The components of (3) and (4) reduce to

$$v\frac{\partial\tilde{u}}{\partial y} = 0, \tag{12a}$$

$$-u\frac{\partial\tilde{u}}{\partial y} + \frac{\partial}{\partial y}\left(\tfrac{1}{2}u^2 + \tfrac{1}{2}v^2 + g'(h_b + h) - \Omega hu\right) = 0, \tag{12b}$$

$$\frac{\partial}{\partial y}(hv) = 0, \tag{12c}$$

where $g' = g\Delta\rho/\rho$ is the reduced gravity, ρ is the density of the active layer, and $\rho - \Delta\rho$ is the density of the deep layer above. Equation (12a) is the depth-averaged equivalent of equation (35) of Colin de Verdière and Schopp (1994), which states that the velocity in the meridional–vertical plane must be parallel to lines of constant absolute angular momentum in zonally symmetric flow. The depth-averaged form (12a) states that for non-zero meridional velocity, $v \neq 0$, the angular momentum must be constant

$$\tilde{u} = u - \tfrac{1}{2}\beta y^2 + 2\Omega(h_b + \tfrac{1}{2}h) = A, \tag{13}$$

where A is constant. Thus the half-layer height of the fluid, $\bar{z} = h_b + \frac{1}{2}h$, traces a line of constant absolute angular momentum. Even in cases where $v \equiv 0$, we will use (13) to close the system (12a)–(12c). Substituting (13) into (12b) yields an exact derivative with respect to y, which may be integrated to obtain a Bernoulli-like equation,

$$\tfrac{1}{2}u^2 + \tfrac{1}{2}v^2 + g'(h_b + h) - \Omega h u = B, \tag{14}$$

where B is the (arbitrary) Bernoulli constant. The $-\Omega h u$ term in (14) is an additional contribution to the pressure created by the complete Coriolis force, and the subsequent change from hydrostatic to quasihydrostatic balance in the vertical momentum equation. Finally, the mass conservation equation (12c) may be integrated to obtain

$$hv = T, \tag{15}$$

where T is the constant meridional transport. Equations (13)–(15) express conservation of angular momentum, Bernoulli energy, and mass respectively. They form an algebraic system of equations that may be combined into a quartic polynomial in u. This must be solved at all points along the y-axis, subject to

$$u(y_0) = U, \quad v(y_0) = V, \quad h(y_0) = H, \tag{16}$$

at some location $y = y_0$. In all cases examined here, only one of the four solutions to the quartic is real at all points in y and satisfies the boundary conditions (16).

We will consider the specific case of a parabolic bottom topography that is half as steep as the ideal topography (7), such that it has the approximate measurements of the channel depicted in Fig. 3,

$$h_b(y) = \frac{y^2}{4R_E}. \tag{17}$$

In Fig. 5 we present a typical solution for fluid crossing the equator over parabolic topography. This may be thought of as a simplistic representation of the AABW entering and exiting the equatorial channel. A comparatively shallow, 200 metres deep, layer of fluid enters flowing directly northwards at $15\,\mathrm{cm\,s^{-1}}$. Gravity keeps the upper surface close to horizontal, so the layer thickens and slows as it approaches the centre of the channel, and then becomes symmetrically swifter and shallower on the opposite site of the equator.

For small density differences ($\Delta\rho/\rho \lesssim 10^{-4}$), the upper surface dips with the topography. We have chosen $g' = 5 \times 10^{-4}\,\mathrm{m^2\,s^{-1}}$ in Fig. 5 to illustrate this. Fig. 6(a) reveals that this is because a large westward velocity is required at the equator to conserve angular momentum (13), and this must be balanced by a gravitational pressure gradient in (14). This westward velocity is much weaker when the complete Coriolis force is included, because in a zonal channel the fluid is subject to less variation in its distance from the rotation axis, as explained in Section 3. As a result, fluid particles flowing across the channel cover a much smaller westward distance as they do so. In the case plotted in Fig. 6, the particle path compares better with the dimensions of the real AABW channel in Fig. 1 when the complete Coriolis force is included. However, this fit is entirely dependent on the choice of inflow velocity V.

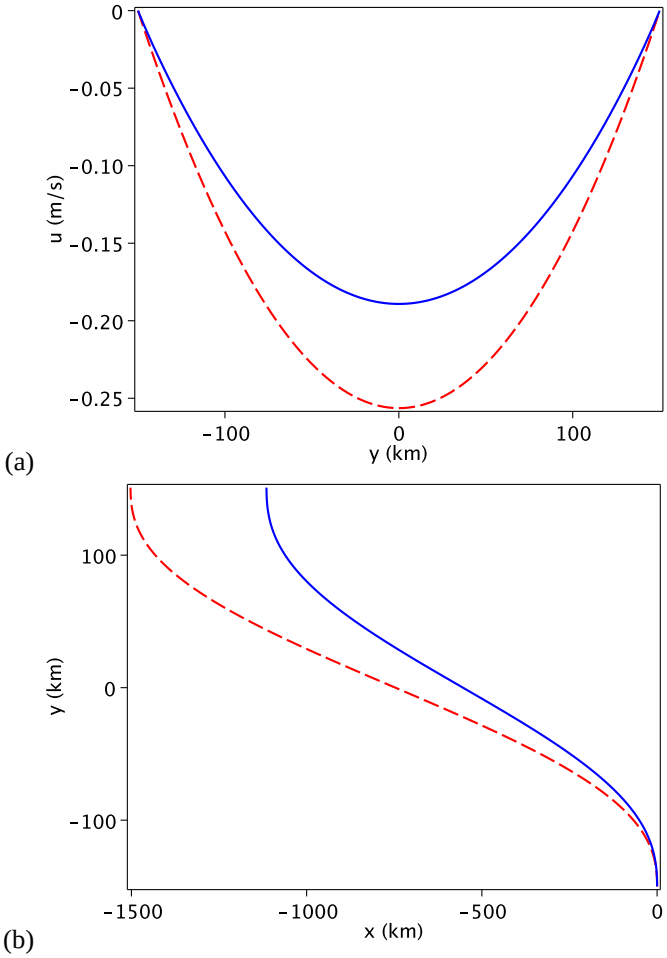

Figure 6: Further plots of the solution presented in Fig. 5. In (a) we show variation of the zonal velocity across the channel, whilst in (b) we show the path of a fluid particle entering at the southern side of the channel. In both cases we plot solutions with (solid lines) and without (dashed lines) the non-traditional component of the Coriolis force.

This solution illustrates the mechanism described in Section 3. When the complete Coriolis is included, the fluid is subject to a smaller change in planetary angular momentum, and so it acquires a smaller relative angular momentum at the equator itself. Equivalently, the fluid acquires a smaller relative vorticity as it crosses the equator. The velocities in Fig. 5 and Fig. 6 are around an order of magnitude larger than those measured in the AABW (c.f. Hall et al., 1997), so the zonal velocity is arguably more realistic when the complete Coriolis force is included. We have chosen a meridional inflow of $V = 0.15\,\mathrm{m\,s^{-1}}$ so that the velocities are of consistent magnitude, and so that the particle paths in Fig. 6 are comparable with the dimensions of the AABW's real bathymetry. Such large velocities may be attributed to the absence of bottom friction and viscosity in this idealised model. The largest vertical velocities attained in the solution are on the order of $10^{-3}\,\mathrm{m\,s^{-1}}$, so the flow does remain approximately horizontal, as required by shallow water theory.

4.2. Vanishing layer depth

A special case of the above solution arises when the layer outcrops from the edge of the channel. This could be a more realistic representation of the flow of the AABW, which tends to lean against the sides of the channel as it traverses the equatorial bathymetry (Hall et al., 1997). In this case, $h = 0$ at $y = y_0$, so there is no meridional transport, $T = 0$, and thus $v \equiv 0$ everywhere. We see from (12a)–(12c) that a stationary solution, $u = v = 0$, $h + h_b =$ constant, is possible. However, we will seek solutions for a zonally-flowing current with zero potential vorticity, satisfying (13). We assume that the AABW adheres to this state to avoid being subject to a symmetric instability (Hua et al., 1997).

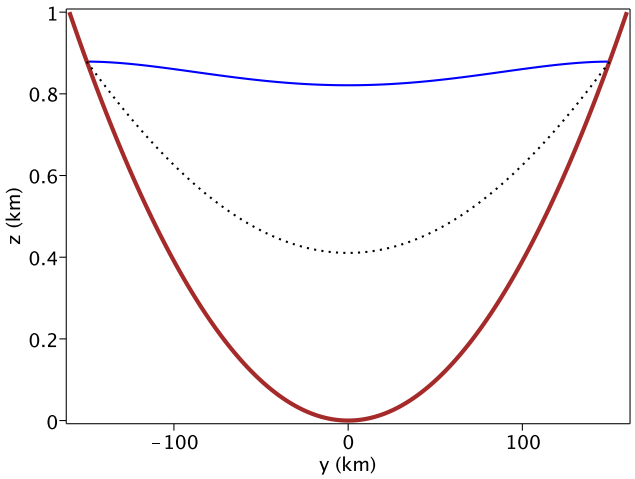

Figure 7: An outcropping solution of (13)–(15), with $y_0 = -150\,\mathrm{km}$, $U = 0\,\mathrm{m\,s^{-1}}$, $V = 0\,\mathrm{m\,s^{-1}}$, $H = 0\,\mathrm{m}$ and $g' = 5 \times 10^{-4}\,\mathrm{m^2\,s^{-1}}$. We plot the bottom topography (thick line), the height of the layer above it (thin line), and the half-layer depth (dotted line).

When $v = 0$, equations (13) and (14) may be combined to form a quadratic polynomial in h. Fig. 7 shows a plot of the layer thickness for similar parameters as those used in Fig. 5, but modified so that the depth vanishes at the edge of the channel. The zonal velocity profile is very similar to that shown in Fig. 6(a).

In this case the fluid is not crossing the equator, but rather flowing westward along the equator. We might expect to observe behavior like this in the AABW over short stretches of the equatorial bathymetry. This solution presents a different interpretation of the rôle of the complete Coriolis force. Including the non-traditional terms leads to smaller westward velocities, and therefore a smaller transport along the channel. Therefore, if the AABW were to exhibit steady, zonally-symmetric flow at some point in the equatorial bathymetry, the complete Coriolis force would actually constrain the amount of fluid transported through the channel.

4.3. Interaction with the upper ocean

We may extend the solution presented in Section 4.1 to include multiple layers of fluid. This allows us to study the interaction of the AABW with overlying layers like the Lower North Atlantic Deep Water (LNADW), which flows southward across the equator above the AABW. Applying the conditions of steady ($\partial/\partial t \equiv 0$), zonally symmetric ($\partial/\partial x \equiv 0$) flow to (3) and (4), the multi-layer shallow water equations may be written as

$$\frac{\partial}{\partial y}\left(u_i - \tfrac{1}{2}\beta y^2 + 2\Omega\left(\eta_{i+1} + \tfrac{1}{2}h_i\right)\right) = 0, \quad (18a)$$

$$\frac{\partial}{\partial y}\left(\tfrac{1}{2}|\mathbf{u}_i|^2 + g\eta_i - \Omega h_i u_i + \frac{1}{\rho_i}\sum_{j=1}^{i-1}\rho_j h_j (g - 2\Omega u_j)\right) = 0, \quad (18b)$$

$$\frac{\partial}{\partial y}(h_i v_i) = 0, \quad (18c)$$

for $i = 1, \ldots, N$. As in the single-layer case, we have written (18a)–(18c) such that they take the form of exact derivatives with respect to y. Integrating yields a system of $3N$ algebraic equations for u_i, v_i, and h_i,

$$u_i - \tfrac{1}{2}\beta y^2 + 2\Omega\left(\eta_{i+1} + \tfrac{1}{2}h_i\right) = A_i, \quad (19a)$$

$$\tfrac{1}{2}u_i^2 + \tfrac{1}{2}v_i^2 + g\eta_i - \Omega h_i u_i + \frac{1}{\rho_i}\sum_{j=1}^{i-1}\rho_j h_j (g - 2\Omega u_j) = B_i, \quad (19b)$$

$$h_i v_i = T_i. \quad (19c)$$

Here A_i, B_i and T_i are determined by imposing

$$u_i(y_0) = U_i, \quad v_i(y_0) = V_i, \quad h_i(y_0) = H_i, \quad (20)$$

at some location $y = y_0$.

In principle, equations (19a)–(19c) may be solved directly to obtain a solution for all y. We see from (19a) that the i^{th} layer will only be substantially influenced by the non-traditional component of the Coriolis force, if there are large variations of the half-layer depth $\overline{z}_i = \eta_{i+1} + \frac{1}{2}h_i$ with y. The surface at $z = \eta_{i+1}$ of the layer below acts as effective topography for the i^{th} layer. It plays an analogous rôle in the multi-layer case to the rôle played by h_b for a single layer. Typically we will only see large deformations in the surface of a given layer η_i when the surface below, η_{i+1}, also has large deformations, and when the density difference between that layer and the layer above is very small, $\sigma_i = (\rho_i - \rho_{i-1})/\rho_i \ll 1$. We quantify what "very small" means in terms of a Froude number in the next subsection. Thus, if the actual bottom topography $h_b = \eta_{N+1}$ forms a channel about the equator, then we only expect fluid in the i^{th} layer to be steered by the channel, and therefore experience strong non-traditional effects, if there are very small density variations between all of the layers below.

In Fig. 8 we plot a solution to (19a)–(19c) with the same parameters as in Fig. 5, but with an overlying southward-flowing layer. This solution is an idealised representation of the AABW flowing north across the equatorial channel, with the southward-flowing LNADW above. The AABW layer is very similar to the single layer shown in Fig. 5 and Fig. 6(a). The upper LNADW layer may influence the AABW only through its contribution to the pressure gradient in (18b). The large westward velocity at the equator, seen in Fig. 6(a), accelerates the

fluid downward via the non-traditional term in the vertical momentum equation (1c). This must be balanced by the gravitational pressure gradient, leading to slight dip in the surfaces of the layers at the equator in Fig. 8. However, this effect is not pronounced unless the density differences at the layer surfaces are very small. In this case the AABW surface is almost flat, so the LNADW is not steered by the channel.

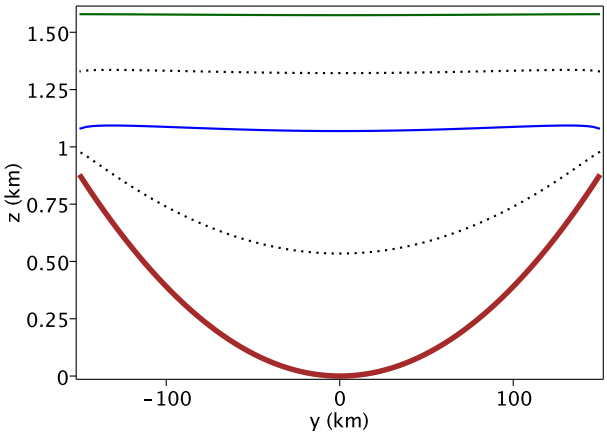

Figure 8: The steady solution for a northward-flowing AABW layer beneath a southward-flowing LNADW layer. Here $y_0 = -150\,\mathrm{km}$, $U_1 = U_2 = 0\,\mathrm{m\,s^{-1}}$, $V_1 = -0.1\,\mathrm{m\,s^{-1}}$, $V_2 = 0.5\,\mathrm{m\,s^{-1}}$, $H_1 = 500\,\mathrm{m}$ and $H_2 = 200\,\mathrm{m}$. The density differences are $\sigma_1 = 10^{-3}$ and $\sigma_2 = 5 \times 10^{-5}$, so the solution is similar to that presented in Fig. 5. We plot the layer surfaces (thin solid lines), the bottom topography (thick solid line) and the half-layer depths (dotted lines).

In Fig. 9 we plot a solution in which the LNADW is steered by the topography, because the density difference between the two active layers is small, $\sigma_2 = (\rho_2 - \rho_1)/\rho_2 = 2.5 \times 10^{-6}$. In this case the AABW surface intersects the channel edges. This can be thought of as a representation of the mid-channel state of the AABW, with the LNADW flowing over the top. The surface of the AABW layer dips towards the equator, providing a gravitational pressure gradient to balance the strong westward flow and the non-traditional vertical acceleration in (18b). The LNADW flows over the channel-shaped AABW-surface, and therefore acquires a smaller westward velocity as it crosses the equator.

For even smaller σ_2, gravitational effects become so weak in the lower layer that the solution jumps to a different physical regime, in which the AABW surface protrudes upward towards the middle of the channel. This configuration is illustrated in Fig. 10, where $\sigma_2 = 1 \times 10^{-6}$. The gravitational pressure gradient due to bending of the internal interface is too small to balance the strong westward flow of the AABW. Instead the LNADW surface must deform to provide this pressure gradient. This is due to the non-traditional contribution to the pressure gradient in (18b), and does not occur under the traditional approximation, where the solution resembles Fig. 9(a) even as $\sigma_2 \to 0$.

We conclude that the upper ocean has a minimal effect of the AABW layer. Whilst it is possible in theory for the shape of the underlying topography to be transmitted to the upper layers, for typical parameters there is almost no deformation of

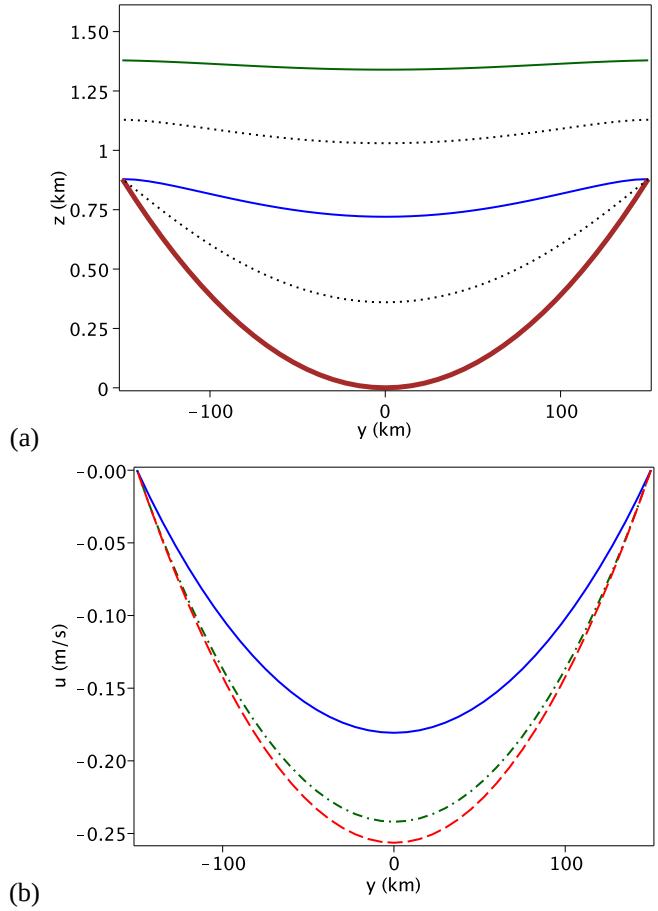

Figure 9: The steady solution for an upper LNADW layer flowing south over an outcropping AABW layer. In panel (a) the plotted curves have the same meaning as in Fig. 8, and the parameters are the same except $V_2 = 0\,\mathrm{m\,s^{-1}}$, $H_2 = 0\,\mathrm{m}$, and $\sigma_2 = 5 \times 10^{-6}$. In panel (b) we plot the zonal velocity profiles in the lower (solid line) and upper (dash-dotted line) layers, and the zonal velocity under the traditional approximation (dashed line), which is identical in both layers.

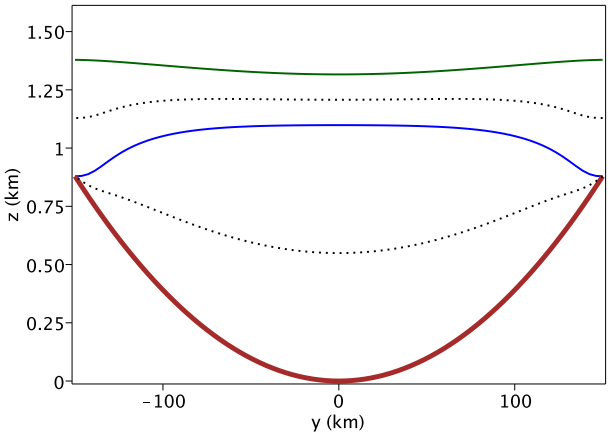

Figure 10: A steady two-layer solution with a very small density difference between the layers, $\sigma_2 = 1 \times 10^{-6}$, and all other parameters matching Fig. 9(a). Under the traditional approximation, the same parameters yield a solution that strongly resembles Fig. 9(a).

the surface of the AABW layer, and therefore the upper layers are not substantially influenced by the complete Coriolis force. In the real AABW we might expect the upper ocean to be steered by the channel if the isopycnals approximately followed the bathymetry, but observations (*e.g.* Hall et al., 1997) suggest that this is typically not the case.

4.4. The small Froude number limit

As discussed in the previous section, the surfaces of the layers will not exhibit large deformations unless the density differences between them are very small. More precisely, the surfaces will be approximately flat as long as the Froude numbers are small,

$$\mathrm{Fr}_i = \frac{\mathcal{U}^2}{\sigma_i g \mathcal{H}} \ll 1, \qquad \sigma_i = \frac{\rho_i - \rho_{i-1}}{\rho_i}, \tag{21}$$

where $\mathcal{U}$ and $\mathcal{H}$ are typical velocity and height scales respectively, and $\sigma_i g$ is the relevant reduced gravity. We show this formally by scaling

$$\mathbf{u}_i = \mathcal{U}\,\hat{\mathbf{u}}_i, \qquad h = \mathcal{H}\,\hat{h}_i, \tag{22}$$

and rewriting (19b) as

$$\hat{\eta}_i + \frac{1}{\rho_i}\sum_{j=1}^{i-1}\rho_j \hat{h}_j + \mathrm{Fr}\left(\tfrac{1}{2}\hat{u}_i^2 + \tfrac{1}{2}\hat{v}_i^2\right) - \delta\,\mathrm{Fr}\left(\tfrac{1}{2}\hat{h}_i\hat{u}_i + \frac{1}{\rho_i}\sum_{j=1}^{i-1}\rho_j \hat{h}_j\hat{u}_j\right) = B_i. \tag{23}$$

A factor of $1/(g\mathcal{H})$ has been absorbed into the constants B_i, and we introduce a measure of the strength of non-traditional effects through

$$\delta = \frac{2\Omega\mathcal{H}}{\mathcal{U}}, \tag{24}$$

the ratio of the non-traditional velocity scale $2\Omega\mathcal{H}$ to the fluid velocity scale $\mathcal{U}$. Assuming $\delta = O(1)$ and $\mathrm{Fr} \ll 1$, the leading-order form of (23) in Fr may be rearranged into

$$\hat{\eta}_i = \tilde{B}_i, \quad \text{for} \quad i = 1, \ldots, N, \tag{25}$$

where the $\tilde{B}_i$ are linear combinations of the B_i.

Returning to dimensional variables and applying the boundary conditions (20), the layer heights are all constants,

$$h_i(y) = H_i, \quad \text{for} \quad i = 1, \ldots, N-1, \tag{26}$$

except for the bottom layer, whose height must vary to keep its upper surface flat,

$$h_N(y) = H_N + h_b(y) - h_b(y_0). \tag{27}$$

This assumes that the lowest layer does not outcrop from the topography. The meridional velocity follows immediately from (19c) for conservation of mass, *i.e.* $v_i = V_i$ for $i < N$, and

$$v_N(y) = \frac{V_N H_N}{H_N + h_b(y) - h_b(y_0)}. \tag{28}$$

Finally, the zonal velocity is unaffected by the non-traditional component of the Coriolis force in all but the lowest layer,

$$u_i(y) = U_i + \tfrac{1}{2}\beta\left(y^2 - y_0^2\right), \qquad \text{for } i = 1, \ldots, N, \tag{29}$$

$$u_N(y) = U_N + \tfrac{1}{2}\beta\left(y^2 - y_0^2\right) - \Omega(h_b(y) - h_b(y_0)) \tag{30}$$

This explicit leading-order solution confirms that, in the case of strongly-stratified layers, the layer surfaces are approximately flat, and only the lowest layer is influenced by the complete Coriolis force, unless the layer surfaces outcrop from the topography.

5. Unsteady flow in a steep-sided channel

The steady-state solutions discussed in Section 4 provide useful insight into the rôle of the complete Coriolis force. However, this raises the question as to whether a cross-equatorial flow would ever evolve into such states. Additionally, we have not discussed how an equatorial channel affects flow from a point far south of the equator to a point far north, which requires a modification of the fluid's potential vorticity. We therefore now consider time-dependent solutions of the one-dimensional shallow water equations, using a steep-sided channel whose dimensions better reflect those of the actual equatorial bathymetry.

5.1. Time-dependent shallow water model of the AABW

We represent the AABW as a single fluid layer that is governed by the non-traditional shallow water equations with a reduced gravity,

$$\frac{\partial u}{\partial t} + \Omega\frac{\partial h}{\partial t} + v\left(\frac{\partial u}{\partial y} - \beta y + 2\Omega\frac{\partial}{\partial y}\left(h_b + \tfrac{1}{2}h\right)\right) = 0, \tag{31a}$$

$$\frac{\partial v}{\partial t} + v\frac{\partial v}{\partial y} + \left(\beta y - 2\Omega\frac{\partial}{\partial y}\left(h_b + \tfrac{1}{2}h\right)\right)u + \frac{\partial}{\partial y}\left(g'(h_b + h) - \Omega h u\right) = 0, \tag{31b}$$

$$\frac{\partial h}{\partial t} + \frac{\partial}{\partial y}(hv) = 0. \tag{31c}$$

We obtain the time-dependent solution to (31a)–(31c) via numerical integration. Equation (31a) contains time derivatives of both u and h, so we rewrite it as a material conservation law for the angular momentum $\tilde{u}$ on an equatorial β-plane (Ripa, 1982, 1997),

$$\frac{\partial \tilde{u}}{\partial t} + v\frac{\partial \tilde{u}}{\partial y} = 0, \quad \tilde{u} = u - \tfrac{1}{2}\beta y^2 + 2\Omega\left(h_b + \tfrac{1}{2}h\right). \tag{32}$$

This is the zonally symmetric form of (5). From (6), the zonally symmetric potential vorticity is

$$q = \frac{\hat{\mathbf{z}}\cdot(\nabla\times\tilde{\mathbf{u}})}{h} = -\frac{1}{h}\frac{\partial \tilde{u}}{\partial y}. \tag{33}$$

Thus in the one-dimensional case, uniformly zero potential vorticity ($q \equiv 0$) is equivalent to constant angular momentum, $\tilde{u}$ = constant. Equation (31b) may also be rewritten as

$$\frac{\partial v}{\partial t} + \frac{\partial \Phi}{\partial y} = u\frac{\partial \tilde{u}}{\partial y}, \quad \Phi = \tfrac{1}{2}u^2 + \tfrac{1}{2}v^2 + g'(h_b + h) - \Omega h u, \quad (34)$$

in terms of $\tilde{u}$ and a modified pressure Φ. The forms of (32) and (34) are more convenient for numerical integration.

5.2. Numerical approach

We prescribe an inflow at the upstream (southern) boundary, $y = y_u$, with a fixed depth $h = H$ and velocity $(u, v) = (U, V)$. In the rest of the domain we prescribe a thin, stationary fluid layer to avoid the computational difficulties associated with the layer outcropping from the dry bed. To avoid an initial discontinuity, the upstream conditions conditions are connected smoothly to the interior of the domain via a short exponential tail, as shown in Fig. 11(a). Following Salmon (2002), we prevent the layer depth from approaching zero by using a modified pressure,

$$\tilde{\Phi} = \tfrac{1}{2}u^2 + \tfrac{1}{2}v^2 - \Omega h u + g'\left[h_b + h - h\left(\frac{h_0}{h}\right)^4\right] \quad (35)$$

The additional term in $\tilde{\Phi}$ becomes large when $h \ll h_0$, preventing the layer thickness from decreasing further, but is negligible in the bulk of the fluid where $h \gg h_0$. The layer thickness is initially set to $h = h_0/2$ away from the southern boundary.

The front of the fluid tends to steepen towards a discontinuity when it encounters such a thin layer, so we include an artificial viscosity in (32) and (34) to maintain numerical stability,

$$\frac{\partial \tilde{u}}{\partial t} = -v\frac{\partial \tilde{u}}{\partial y} - ru + \frac{\nu_n}{h}\frac{\partial}{\partial y}\left(h\frac{\partial v}{\partial y}\right), \quad (36)$$

$$\frac{\partial v}{\partial t} = u\frac{\partial \tilde{u}}{\partial y} - \frac{\partial \tilde{\Phi}}{\partial y} - rv + \frac{\nu_n}{h}\frac{\partial}{\partial y}\left(h\frac{\partial v}{\partial y}\right). \quad (37)$$

The form of the viscosity has been chosen to conserve momentum (see Shchepetkin and O'Brien, 1996), whilst the term proportional to $r(y, t)$ represents the leading-order effect of bottom friction. Equations (36) and (37) serve as the basis of our numerical solution, along with the mass continuity equation (31c), which we rearrange into

$$\frac{\partial h}{\partial t} = -\frac{\partial}{\partial y}(hv). \quad (38)$$

This model is not intended to accurately represent the effects of dissipation on an equatorial current. The numerical viscosity serves only to damp spurious oscillations arising due to the coarseness of the discretisation, and the bottom friction term offers an idealised representation of the modification of potential vorticity by dissipative processes. Pedlosky (1987) showed that a bottom Ekman layer may be represented in the shallow water equations as a linear Rayleigh friction with coefficient $r \sim (fA_z)^{1/2}/h$, where A_z is the vertical eddy viscosity. The Coriolis parameter f varies as $f \approx \beta y$ on the equatorial β-plane, so we define r as

$$r(y, t) = \kappa_f\left(\frac{H}{h}\right)\left|\frac{y}{y_u}\right|^{\frac{1}{2}}. \quad (39)$$

The time scale for frictional dissipation at $y = y_u$ is $\tau_f \sim 1/\kappa_f$. This formula for r was derived using the traditional approximation, and the Ekman layer can be substantially altered by the inclusion of the complete Coriolis force (Leibovich and Lele, 1985). Equation (39) becomes especially dubious close to the equator, where $f \to 0$,because the leading-order balance between Coriolis and viscous forces in the Ekman layer breaks down. In the limit of vanishingly small Rossby number, the fluid should form Taylor columns aligned with the axis of rotation, and therefore parallel to the Earth's surface at the equator. Our shallow water equations retain the assumption of columnar motion close to the equator, on the basis that this is consistent with the shallow-layer approximation, and because the stratification of the real ocean makes this a more appropriate model of a cross-equatorial current. A parametrisation of bottom friction applicable to this situation has not been formally derived, so we use (39) as a simple mechanism for potential vorticity modification. Removing the explicit dependence of r on y does not lead to any qualitative changes in our results.

We represent the bathymetry close to the equator using an idealised steep-sided channel that is qualitatively similar to the averaged bathymery shown in Fig. 3, but which flattens off away from the equator. Specifically, we use a channel of the form

$$h_b(y) = h_b^{(0)}\left[1 - \exp\left(\left|\frac{y}{y_w}\right|^n\right)\right], \quad (40)$$

which defines a channel of height $h_b^{(0)}$ and half-width y_w. For the solutions presented below, we use $h_b^{(0)} = 700\,\mathrm{m}$, $y_w = 125\,\mathrm{km}$ and $n = 4$. Further details of our numerical scheme may be found in Appendix A.

5.3. Results

In all of the solutions discussed here, the upstream conditions are $u = U = 0$, $v = V = 10\,\mathrm{cm\,s^{-1}}$, and $h = H = 300\,\mathrm{m}$, and the reduced gravity is $g' = 5 \times 10^{-4}\,\mathrm{m\,s^{-2}}$. We discretise the solutions using $M = 501$ points from the upstream position $y_u = -250\,\mathrm{km}$ to the downstream position $y_d = +250\,\mathrm{km}$, giving a grid spacing of $\Delta y = 1\,\mathrm{km}$. Sponge layers of width $S = 30$ gridpoints occupy the regions $220\,\mathrm{km} \le |y| \le 250\,\mathrm{km}$ at both edges of the domain (see Appendix A). We use $h_0 = 50\,\mathrm{m}$, so the initial layer thickness away from the southern boundary is 25 m, and the numerical viscosity coefficient is $\nu_n = 200\,\mathrm{m^2\,s^{-1}}$.

In Fig. 11 we plot the computed solution to (36)–(38) without bottom friction ($\kappa_f = 0$). The current fills the equatorial channel, and eventually tends towards the steady state shown in Fig. 11(b), where it closely resembles the analytical solution obtained via the method of Section 4.1. The only pronounced discrepancy lies close to the northern boundary, where the northern sponge layer damps the computed solution away from the analytical solution. Making the traditional approximation, *i.e.* neglecting all terms multiplied by Ω in (36)–(37),

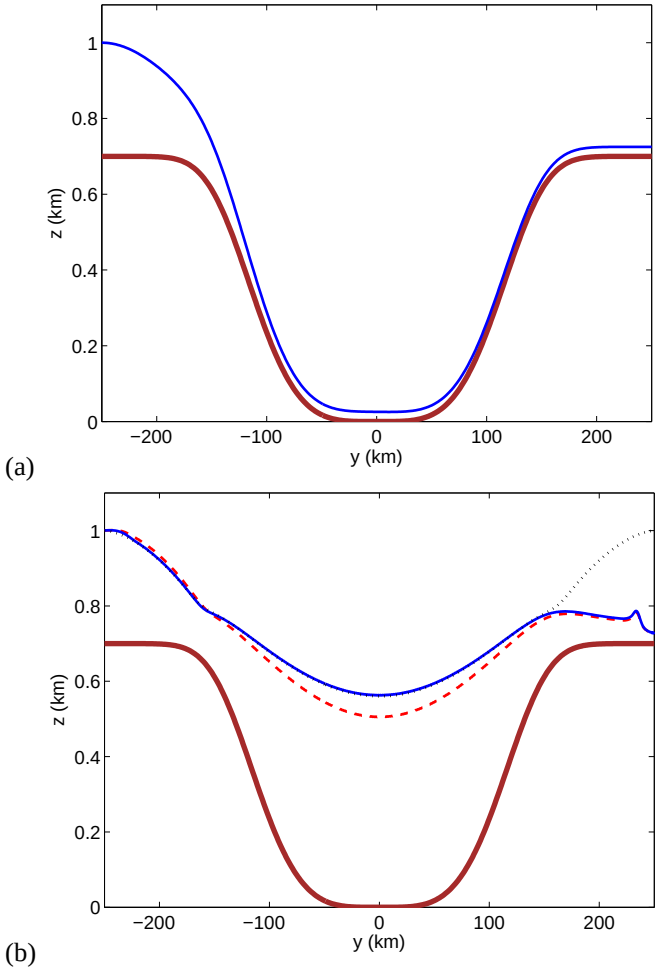

Figure 11: Snapshots of the computed solution to (31a)–(31c) at (a) $t = 0$ and (b) $t = 4000$ days, in the absence of friction ($\kappa_f = 0$). The thick solid line marks the height of the bottom topography, and the dotted line shows the steady solution calculated via the method of Section 4.1, including the complete Coriolis force. The height of the fluid surface is plotted under the traditional approximation (dashed line) and including the complete Coriolis force (thin solid line).

leads to the fluid layer being somewhat shallower in the equatorial channel, but the solution is otherwise almost identical.

Fig. 12 shows the corresponding steady solution for strong frictional dissipation ($\kappa_f = 3\times10^{-2}\,\text{days}^{-1}$). Now the fluid surface no longer dips at the equator, but instead tends to slope downwards to the north, so that the gravitational pressure gradient partly balances the bottom friction term in (37). Including the complete Coriolis force makes almost no difference to this case.

For fluid to travel from far south of the equator to far north of the equator, its potential vorticity must be modified by the action of dissipation, as otherwise it must acquire a prohibitively large relative vorticity (Edwards and Pedlosky, 1998). Including friction in (36) allows the fluid to change its angular momentum $\tilde{u}$, and therefore its potential vorticity, as it crosses the equator. In Fig. 13 we plot the steady-state relative vorticity profiles for several values of the friction parameter κ_f. When $\kappa_f \lesssim 10^{-3}\,\text{days}^{-1}$, $\tilde{u}$ is approximately constant, and so there is

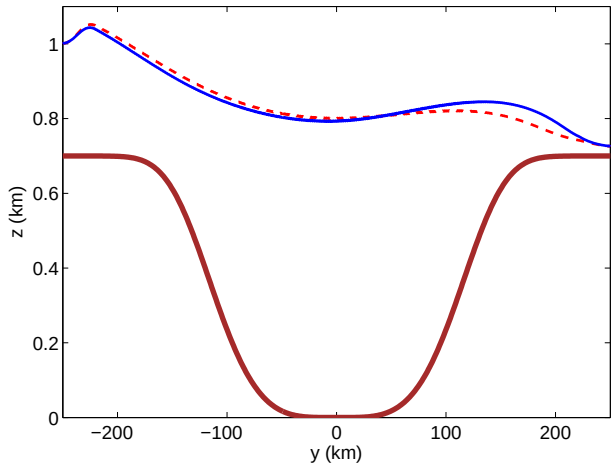

Figure 12: Computed steady-state solution to (31a)–(31c) with moderately strong bottom friction, $\kappa_f = 3\times10^{-2}\,\text{days}^{-1}$. The height of the fluid surface is plotted under the traditional approximation (dashed line) and including the complete Coriolis force (thin solid line), and the thick solid line marks the height of the bottom topography.

a large change in relative vorticity across the channel. As predicted in Section 4, the effect of including the complete Coriolis force is most pronounced where the topographic gradients are largest. We see from the solution for $\kappa_f = 3\times10^{-3}\,\text{days}^{-1}$ that fluid moving from the southern slope to the northern slope of the channel (from $y \approx -100$ km to $y \approx +100$ km) requires a much smaller change in relative vorticity when the complete Coriolis force is accounted for, around 30% to 40% less in this case. However, fluid moving beyond the edges of the channel, from far south of the equator to far north, experiences the same change in relative vorticity regardless of whether the complete Coriolis force is included.

A larger κ_f allows friction to modify the fluid's potential vorticity more readily, so the fluid no longer requires such a large change in its relative vorticity. In Fig. 14(a) we plot the change $\Delta\zeta$ in the relative vorticity as fluid moves from $y = -200$ km to $y = +200$ km, over a range of values of κ_f. The solution changes rapidly from a state of zero potential vorticity at $\kappa_f \lesssim 10^{-2}\,\text{days}^{-1}$, to a friction-dominated state with $\Delta\zeta \approx 0$ at $\kappa_f \gtrsim 5\times10^{-1}\,\text{days}^{-1}$. The influence of the complete Coriolis force is less pronounced at larger values of κ_f, even over large topographic gradients, and $\Delta\zeta$ is almost identical with or without the complete Coriolis force.

In Fig. 14(b) we plot the cross-equatorial transport over the same range of κ_f. At $\kappa_f \approx 10^{-2}\,\text{days}^{-1}$ there is a very rapid drop in the transport. This corresponds to a rapid change in the shape of the fluid surface, characterised by a change from that shown in Fig. 11(b) to that shown in Fig. 12. The transport increases again to a local maximum at $\kappa_f \approx 3\times10^{-1}\,\text{days}^{-1}$, and finally approaches zero when $\kappa_f \gtrsim 5\times10^{-1}\,\text{days}^{-1}$. This behaviour is due to a separation between the scales over which frictional effects are important in (36) and (37). In (37), friction becomes comparable to advection when

$$\kappa_f \left(\frac{H}{h}\right)\left|\frac{y}{y_u}\right|^{\frac{1}{2}} v \sim v\frac{\partial v}{\partial y}, \quad \text{or} \quad \kappa_f \sim \frac{V^2}{VL} \approx 1.7\times10^{-2}\,\text{days}^{-1}, \quad (41)$$

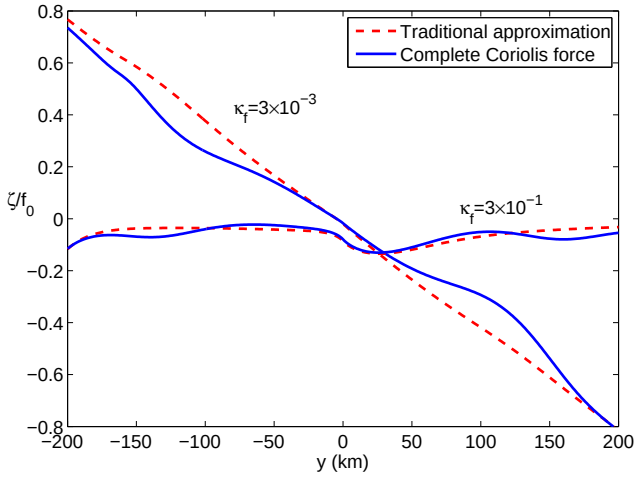

Figure 13: Plots of the steady-state relative vorticity profile across the channel, illustrating the contrast between the cases of strong friction ($\kappa_f = 3 \times 10^{-1}\,\text{days}^{-1}$) and weak friction ($\kappa_f = 3 \times 10^{-3}\,\text{days}^{-1}$). The relative vorticity ζ is scaled by the magnitude of the upstream planetary vorticity, $|f_0| = 2\Omega \sin(|y_u|/R_E)$.

where $L = y_d - y_u$ is the length of the domain. This agrees approximately with the rapid change in the cross-equatorial transport and the shape of the fluid surface. In (36), friction becomes comparable to the upstream angular momentum when

$$\kappa_f \left(\frac{H}{h}\right)\left|\frac{y}{y_u}\right|^{\frac{1}{2}} u \sim u\frac{\partial \tilde{u}}{\partial y}, \quad \text{or} \quad \kappa_f \sim \beta|y_u| \approx 5 \times 10^{-1}\,\text{days}^{-1}. \quad (42)$$

This is consistent with Fig. 14(a), as $\Delta\zeta \approx 0$ when $\kappa_f \gtrsim 5 \times 10^{-1}\,\text{days}^{-1}$.

As stated earler, the sponge layers at the boundaries of the computational domain allow for some variation in the effective boundary conditions in the solution. Our solutions tend to approach a state in which $\Delta\zeta$ is almost identical with or without non-traditional effects, but the cross-equatorial transport becomes larger when non-traditional effects are included. This result is consistent over all values of κ_f, though for $\kappa_f \gtrsim 5 \times 10^{-1}\,\text{days}^{-1}$ the difference between the transports becomes vanishingly small. We conclude that for a given modification of the relative or potential vorticity, a stronger cross-equatorial flow is possible when the complete Coriolis force is included.

6. Cross-equatorial geostrophic adjustment

In the preceding sections we focused on the rôle that the combination of the complete Coriolis force and channel-like equatorial topography plays in cross-equatorial transport of the AABW. In this section we consider a body of fluid that lies initially at rest in the southern hemisphere, and subsequently adjusts towards a state of geostrophic balance by radiating energy in the form of inertia-gravity waves. This problem was first studied by Killworth (1991), who showed that a fluid's ability to adjust across the equator is severly constrained by the change in sign of f. Geostrophic adjustment is likely to be responsible

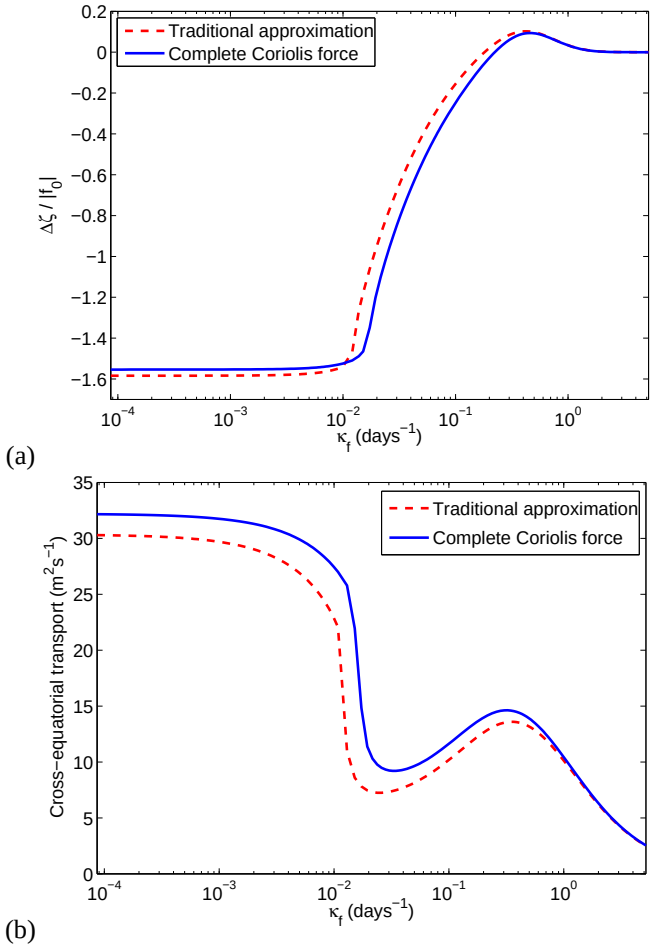

Figure 14: (a) the computed change in relative vorticity, and (b) the steady-state cross-equatorial transport, with the complete Coriolis force (solid lines) and under the traditional approximation (dashed lines). The change in relative vorticity is calculated as $\Delta\zeta = \zeta(y = +200\,\text{km}) - \zeta(y = -200\,\text{km})$, and is scaled by the magnitude of the upstream planetary vorticity, $|f_0| = 2\Omega \sin(|y_u|/R_E)$.

for a proportion of the cross-equatorial flow of the AABW. We find that including the complete Coriolis force increases both the cross-equatorial transport and the distance the fluid reaches in the northern hemisphere. For simplicity, we will illustrate this with a flat topography ($h_b \equiv 0$).

6.1. *The one-dimensional geostrophic adjustment problem*

We restrict our attention to a one-dimensional adjustment problem, so the fluid is governed by (31a)–(31c). In the absence of topography ($h_b = 0$) it is convenient to non-dimensionalise these equations by setting

$$\mathbf{u} = \mathcal{U}\,\hat{\mathbf{u}}, \quad h = \mathcal{H}\,\hat{h}, \quad y = R_d\,\hat{y}, \quad t = \frac{R_d}{\mathcal{U}}\,\hat{t}, \quad (43)$$

where $\mathcal{H}$ is a vertical lengthscale, $\mathcal{U} = \sqrt{g'\mathcal{H}}$ is the characteristic wave speed base on the reduced gravity, and $R_d = \sqrt{\mathcal{U}/2\beta}$ is the equatorial radius of deformation, modified slightly from (10) to match the convention used by Killworth (1991). We

henceforth drop the hat ˆ notation for dimensionless variables. Under this non-dimensionalisation, (31a)–(31c) reduce to

$$\frac{\partial u}{\partial t} + \delta\frac{\partial h}{\partial t} + v\left(\frac{\partial u}{\partial y} - \tfrac{1}{2}y + \delta\frac{\partial h}{\partial y}\right) = 0, \qquad (44a)$$

$$\frac{\partial v}{\partial t} + v\frac{\partial v}{\partial y} + \left(\tfrac{1}{2}y - \delta\frac{\partial h}{\partial y}\right)u + \frac{\partial}{\partial y}(h - \delta h u) = 0, \qquad (44b)$$

$$\frac{\partial h}{\partial t} + \frac{\partial}{\partial y}(hv) = 0, \qquad (44c)$$

where $\delta = \Omega\sqrt{\mathcal{H}/g'}$ is modified from its earlier definition in (10) to match the conventions used by Killworth (1991).

Fig. 15 shows a typical initial state for the one-dimensional geostrophic adjustment problem. The bulk of the fluid lies in the southern hemisphere, with a layer of finite depth h_0 projecting north across the equator, and the velocity is initially zero everywhere. We use an initial height profile of the form

$$h(y,0) = h_0 + \frac{1-h_0}{2}\left[1 + \tanh\left(\frac{Y-y}{W}\right)\right], \qquad (45)$$

such that $h \to 1$ as $y \to -\infty$ and $h \to h_0$ as $y \to \infty$. The adjusted state is strongly dependent on the initial position Y of the front that marks the northern boundary of the fluid, whilst W measures the distance over which the height drops from 1 to h_0, and is fixed at $W = 0.1$ in our solutions. Killworth (1991) obtained a quasi-analytical solution to the case where $h_0 = 0$ under the traditional approximation, but the inclusion of non-traditional terms renders this intractable. We therefore compute the adjusted state by solving an initial value problem for the system (44). We use a finite value $h_0 > 0$ to avoid computational issues associated with the fluid surface intersecting the bottom topography. We describe our numerical scheme in detail in Appendix B.

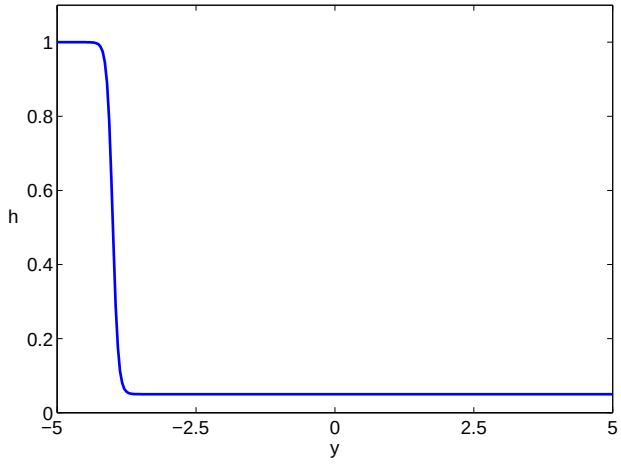

Figure 15: A typical initial state for the cross-equatorial geostrophic adjustment problem. In this example $h_0 = 0.05$ and $Y = -1.9$.

6.2. Results

Fig. 16 shows the adjusted height and zonal velocity reached from the initial condition shown in Fig. 15, corresponding to

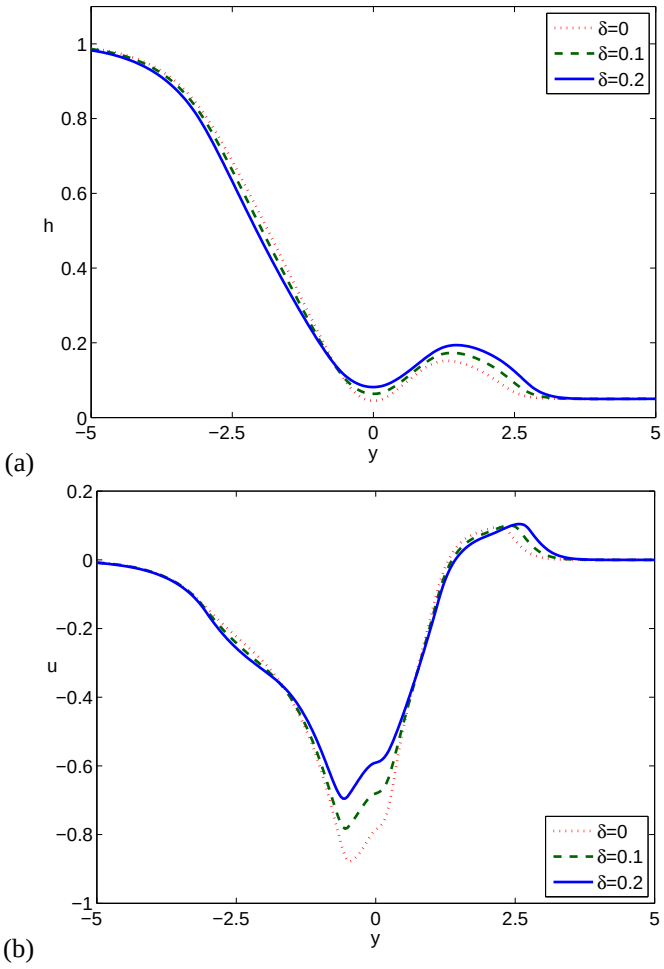

Figure 16: Adjusted (a) height and (b) zonal velocity for the initial height profile shown in Fig. 15, for various values of the non-traditional parameter δ. The time-dependent solution has been calculated on a grid of 1025 points, and then averaged over the interval from $t = 800$ and $t = 1000$ to remove equatorially trapped waves.

(45) with $Y = -1.9$. The adjusted meridional velocity is zero everywhere. Equatorially trapped waves prevent the solution from ever reaching a true steady state, so we plot the averages of the instantaneous profiles over the interval from $t = 800$ and $t = 1000$. For a given initial condition, the adjusted state depends only on the non-traditional parameter δ. Using $\Omega = 10^{-4}\,\mathrm{rad\,s^{-1}}$ and $\mathcal{H} = 1000\,\mathrm{m}$, $\delta = 0.1$ corresponds to $g' = 10^{-3}\,\mathrm{m\,s^{-2}}$, and $\delta = 0.2$ corresponds to $g' = 2.5\times10^{-4}\,\mathrm{m\,s^{-2}}$. These values give length scales for the flow of $R_d = 148\,\mathrm{km}$ and $R_d = 105\,\mathrm{km}$, respectively. This adjusted state is typical when the initial front position Y is sufficiently close to the equator to permit cross-equatorial flow. The fluid depth has a local minimum very close to the equator, leading to a strong westward jet at the equator and a weaker eastward jet north of the equator. Including the complete Coriolis force leads to a larger volume of fluid crossing the equator, and penetrating further into the northern hemisphere. This corresponds to a weaker westward equatorial jet and a slightly stronger eastward jet north of the equator.

The adjusted state varies strongly with Y, the position of

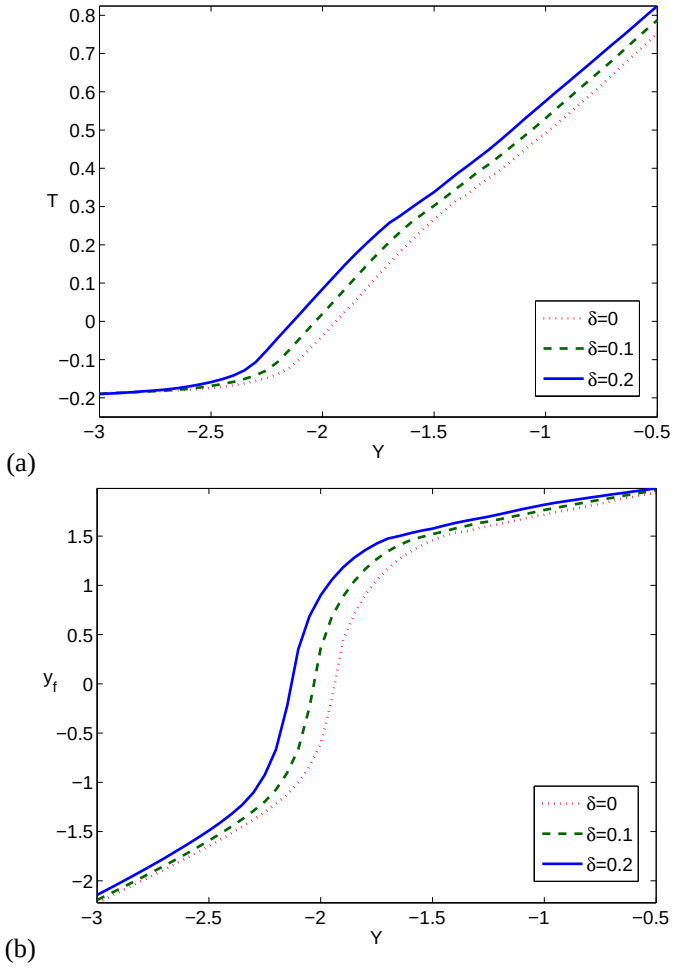

Figure 17: (a) Cross-equatorial transport, T, and (b) final position of the initial front, y_f, plotted as functions of the initial position of the front, Y. We have constructed the plots using the long-time averages of the numerical solution for a range of values of Y. In all cases we have take $h_0 = 0.05$ and used a grid of $N = 1025$ points.

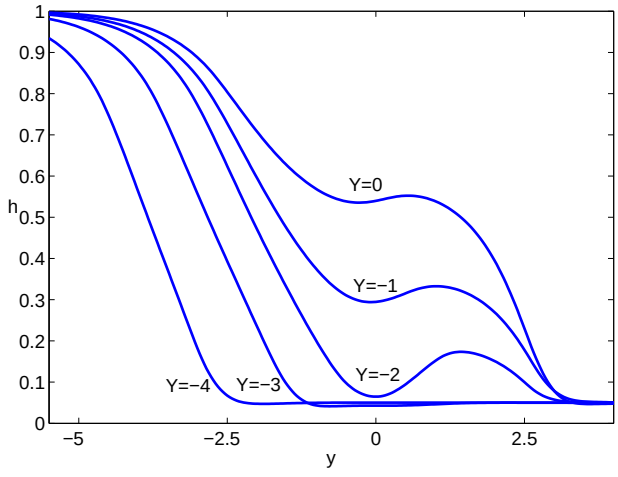

Figure 18: Adjusted height profiles for $\delta = 0.2$, $h = 0.05$, $N = 1025$, and, from left to right, $Y = -4$, $Y = -3$, $Y = -2$, $Y = -1$ and $Y = 0$. Non-traditional effects are most prominent in the $Y = 2$ case, when the depth has a pronounced minimum at the equator.

the front in the initial conditions. Fig. 17 shows the computed cross-equatorial transport T, and final position y_f, of fluid that lies initially at the front $y = Y$. We define y_f by

$$\int_{y_f}^{\infty} h_a(y)\,\mathrm{d}y = \int_{Y}^{\infty} h\,(y, t = 0)\,\mathrm{d}y, \tag{46}$$

where $h_a(y)$ denotes the adjusted height field, and we define the cross-equatorial transport by

$$T = \int_0^{y_f} h_a(y)\,\mathrm{d}y = \int_0^{\infty} h_a(y)\,\mathrm{d}y - \int_Y^{\infty} h\,(y, t = 0)\,\mathrm{d}y. \tag{47}$$

This cross-equatorial transport will be negative if the final position of the front lies south of the equator. This transport T then gives the additional volume of fluid required in the northern hemisphere to allow fluid from $y = Y$ to reach the equator.

Fig. 17 shows that including the complete Coriolis force leads to a larger cross-equatorial transport, T, and a deeper penetration y_f into the northern hemisphere for all starting positions Y. This is most pronounced in the range $-2.5 < Y < -1.5$, where including the complete Coriolis force allows fluid to penetrate up to 2 deformation radii further than it does under the traditional approximation. This is most easily understood in terms of the fluid's angular momentum. Rewriting (44a) as a material derivative, as we did with (32), we obtain

$$\frac{\mathrm{D}\tilde{u}}{\mathrm{D}t} = 0, \quad \tilde{u} = u - \tfrac{1}{4}y^2 + \delta h, \tag{48}$$

where $\mathrm{D}/\mathrm{D}t \equiv \partial/\partial t + v\partial/\partial y$, and $\tilde{u}$ is the dimensionless angular momentum. Thus $\tilde{u}$ is conserved following the fluid. Under the traditional approximation ($\delta = 0$), the planetary angular momentum $\tilde{u}_p = -\frac{1}{4}y^2$ increases towards the equator. To cross the equator, fluid starting at rest must generate a large negative zonal velocity u, which may be thought of as a relative angular momentum, to balance the increase in $\tilde{u}_p$. Including the complete Coriolis force ($\delta \neq 0$) accounts for the fact that changing a fluid column's depth changes the average distance of the fluid parcels within it from the axis of rotation, and therefore changes their average planetary angular momentum $\tilde{u}_p = -\frac{1}{4}y^2 + \delta h$. A layer of fluid crossing the equator will thus experience a smaller change in $\tilde{u}_p$ if its thickness decreases towards the equator. In Fig. 18 we plot the adjusted depth profiles for several values of Y. In general, the surface of the layer tends to dip towards the equator, reducing the fluid's planetary angular momentum and thereby facilitating cross-equatorial flow. In particular, the dip is most pronounced, whilst still centred on the equator, around $Y \approx -2$. This explains the prominence of non-traditional effects in the range $-2.5 < Y < -1.5$.

The adjusted state also strongly depends on the initial depth h_0 to the north of the front. Killworth (1991) showed that if $h_0 \lesssim 0.04$ then an analytical steady-state solution may not exist for $-1.9 \lesssim Y \lesssim -1.5$. Computing the time-dependent solution with similar parameters leads to adjusted states in which the depth approaches zero at the equator. In Fig. 19 we plot the adjusted height profile for $h_0 = 0.01$ and $Y = -2.0$, computed with a high resolution (8193 gridpoints). Close to $y = 0$, the depth h tends rapidly to zero with increasing resolution. In the

example shown in Fig. 19, all three curves have minima below 10^{-53}, and the $\delta = 0$ curve falls below 10^{-118}. The adaptive time-stepping of our numerical scheme allows us to compute the solution at such small layer thicknesses without h intersecting the ocean bed. The appearance of these extremely small values of h suggest that we should seek a solution in the form of two disconnected regions separated by an interval of vanishing depth.

Note that $Y = -2.0$ lies slightly outside the range determined by Killworth (1991) to possess no steady-state solutions, because our initial condition (45) contains a sharp slope rather than a true discontinuity. This solution suggests that in the exact adjusted state, the fluid should separate into two separate masses on either side of the equator. This cannot be described using the formulation of Killworth (1991), because the analytical solution depends on a continuous map $y \to y_0$ from the position of a given fluid element in the adjusted state, y, to the position of that fluid element in the initial state, y_0. This map becomes discontinuous if the fluid splits into two separate water masses in the adjusted state, so the analytical solution cannot be calculated.

Fig. 20 shows the final position y_f of the front for values of the initial northern depth in the range $0.01 \leq h_0 \leq 1$. This shows that fluid can penetrate further into the northern hemisphere when the complete Coriolis force is included, regardless of the values of h_0 or Y. The increase in the penetration distance y_f is most pronounced for small h_0, where the adjusted height dips further towards the equator. The corresponding reduction in the planetary angular momentum facilitates cross-equatorial flow when the complete Coriolis force is included, as described above. However, this difference vanishes as $h_0 \to 0$, where all of the curves in Fig. 20 appear to converge just above $y_f = 2$. This agrees with Killworth's (1991) finding that fluid can only penetrate around two deformation radii north of the equator via the process of geostrophic adjustment alone.

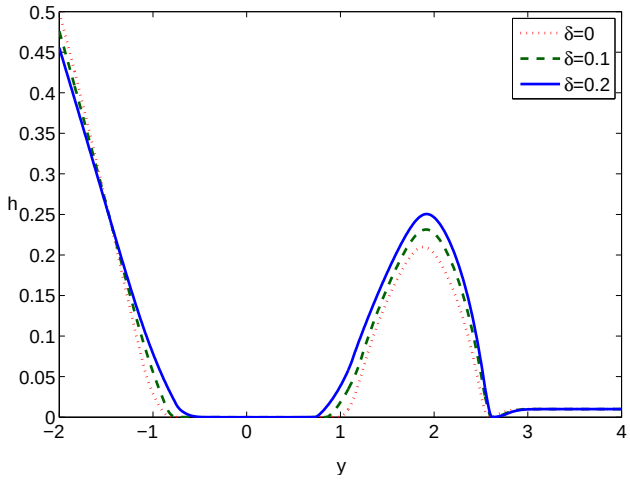

Figure 19: Adjusted height profile for $Y = -2.0$ and $h_0 = 0.01$, for different values of the non-traditional parameter, δ. This solution has been computed at a high resolution using 8193 gridpoints. Close to $y = 0$, h becomes vanishingly small with increasing resolution, indicating that the fluid has split into separate water masses on either side of the equator.

7. Conclusion

We have considered the rôle of the "non-traditional" component of the Coriolis force in cross-equatorial transport of ocean currents, with particular emphasis on the AABW. Our approach does not attempt to describe completely the physics of interhemispheric exchange, but rather focuses on highly idealised scenarios to isolate key features. Specifically, we have focused on the interaction of non-traditional Coriolis effects with channel-like equatorial topography, and shown that this combination should facilitate the crossing of the AABW. This may explain why so much of the AABW penetrates into the northern hemisphere, whilst many other equatorial currents are blocked by the equator.

The most important contribution of the non-traditional component of the Coriolis force lies in the potential vorticity, which is well established across the oceanographic and atmospheric sciences as a critical dynamical variable (*e.g.* Müller, 1995). It is because of this contribution that the effect of the non-traditional component far exceeds the scaling estimates described in Section 3. In the presence of a zonal equatorial channel, the non-traditional term may balance the change in $f \approx \beta y$ as fluid crosses the equator. This means that the fluid need not acquire as much relative vorticity in crossing to the northern hemisphere. The difficulty in acquiring relative vorticity has been shown to inhibit cross-equatorial flow (Killworth, 1991).

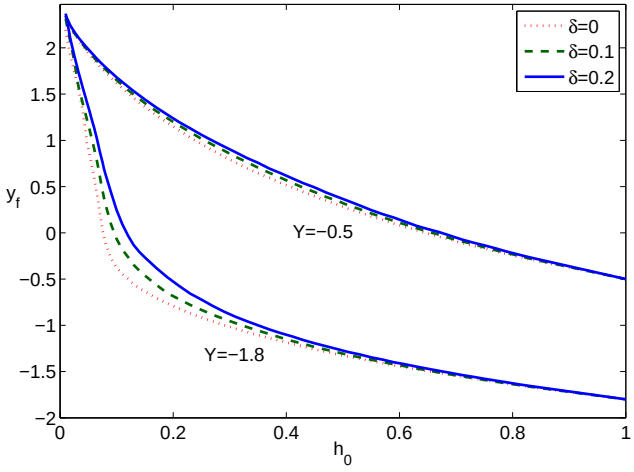

Figure 20: Position of the front after adjustment, y_f, plotted for a range of downstream depths h_0, and for two different starting positions, $Y = -2.0$ and $Y = -0.5$. All solutions have been calculated using $N = 1025$ gridpoints.

The analytical solutions of Section 4 provide two descriptions of the influence of the complete Coriolis force on the AABW. The solutions that describe a current crossing a zonal equatorial channel, such as those in Section 4.1, illustrate the mechanism described above. Less relative vorticity is generated as the fluid crosses the equator because the non-traditional terms partially balance the change in f. However, the actual cross-equatorial transport is identical in both the traditional and non-traditional cases. The alternative solution of Section 4.2, in which the layer outcrops from the edges of the channel, may

be thought of as a snapshot of the AABW as it traverses the equatorial channel. In this case the flow is purely zonal, and the including non-traditional effects leads to smaller westward velocities. Thus, in this case the complete Coriolis force reduces the transport of the current.

In Section 5 we considered the time-dependent flow of a current northward across the equator, through a channel resembling the bathymetry of Fig. 3(a). In the absence of friction, the computed steady state shown in Fig. 11(b) closely resembles the analytical solution obtained in Section 4. This scenario is not entirely realistic, as the AABW flows through and crosses an equatorial channel, rather than traversing it from edge to edge. However, the solution illustrates that the channel need not be the perfect parabola defined in (7) to facilitate an equatorial crossing. In fact, as Fig. 13 shows, having steep slopes at the edges of the channel and an almost-flat section in the middle will greatly reduce the relative vorticity required to cross the equator.

Whilst these solutions shed light on the interaction of the non-traditional component of the Coriolis force with sharply-varying topography, fluid that exits the equatorial channel must acquire the same large relative vorticity that it would under the traditional approximation. We have therefore included a simple representation of bottom friction in our numerical solutions, which allows the fluid to modify its potential vorticity as it crosses the equator. Stronger frictional dissipation leads to a smaller change in the relative vorticity as the fluid crosses the equator, and this change is almost identical when when the complete Coriolis force is included. However, for an approximately identical change in the relative vorticity, the cross-equatorial transport is always larger when the complete Coriolis force is included.

Finally, we revisited the one-dimensional cross-equatorial geostrophic adjustment problem of Killworth (1991). Including the complete Coriolis force hinders the analytical approach to this problem, so we used the high-resolution total variation diminishing scheme of Kurganov and Tadmor (2000) to obtain accurate solutions to the inviscid shallow water equations. It would be of little value to apply this scheme to the cross-equatorial flow problem of Section 5, as the explicit friction and sponge layer damping negate any advantage conferred by a total variation dimishing scheme.

The non-traditional component of the Coriolis force allows more fluid to adjust further across the equator, regardless of the initial position of the front, as shown in Fig. 17, or the initial northern depth, as shown in Fig. 20. Each fluid parcel must conserve angular momentum (48) as it crosses the equator, which requires a large westward velocity to balance the increase in planetary angular momentum. Including the complete Coriolis force accounts for the fact that changes in the fluid depth correspond to changes in the average distance of the fluid in a column from the axis of rotation, and therefore contribute to the angular momentum. The depth of the adjusted fluid layer tends to dip towards the equator, reducing the westward velocity required to cross the equator. The fluid's planetary angular momentum would be reduced further in the presence of a channel straddling the equator, so we expect that the AABW's bathymetry would lead to an even larger cross-equatorial transport by geostrophic adjustment if the complete Coriolis force was included.

This study has neglected zonal variations, which are likely to be very important in the actual evolution of the AABW. The one-dimensional solutions presented here may be unstable to zonal perturbations, and indeed there is no reason to expect that a two-dimensional solution should ever reach a steady state. Indeed, Hall et al. (1997) found that the AABW exhibits substantial time-variability. The generation of relative vorticity as the current crosses the equator may lead to the formation of eddies capable of pumping fluid back into the southern hemisphere, though this may be offset by modification of the potential vorticity by dissipation. An investigation of the rôle of the complete Coriolis force in two-dimensional transport of cross-equatorial currents is ongoing.

Although we can not claim to describe accurately the behaviour of the AABW using the idealised conditions presented in this paper, we still obtain a useful insight into the rôle of the complete Coriolis force. It is interesting to see that the non-traditional component of the Coriolis force substantially influences the solutions, where in previous studies it has invariably been neglected. This work confirms that including the complete Coriolis force is vital for an accurate representation of abyssal current flows close to the equator.

Appendix A. Numerical scheme employed in §5

We approximate the solution in the region $[y_u, y_d]$, where y_d is the downstream (northern) boundary, using discrete values $\{\tilde{u}_m(t), v_m(t), h_m(t)\}$ at the regularly spaced points y_m for $m = 1, \ldots, M$. We approximate the y-derivatives on the right hand sides of (36)–(38) using second-order centred finite differences, and integrate forward in time using the fourth-order Runge-Kutta scheme. This requires recalculation of the zonal velocity u from the angular momentum $\tilde{u}$ at each time step. We halt the integration when the solution reaches a steady state, as defined by the pointwise variations of all variables $\{\tilde{u}_m, v_m, h_m\}$ being less than 0.1% over a period of 100 days.

The inclusion of a second-order term in (37) complicates this problem, as it necessitates additional boundary conditions for $\tilde{u}$, v and h. In fact, even without this term, the prescription of boundary conditions for $\tilde{u}$, v and h at the upstream edge of the domain is somewhat difficult. The two-dimensional non-rotating shallow water equations have characteristics with speeds v and $v \pm \sqrt{g'h}$ (*e.g.* Whitham, 1974), so for small velocities $|v| < \sqrt{g'h}$ there are characteristics propagating in both directions. Information is then able to propagate towards both the northern and southern boundaries, but the solution cannot describe the behaviour of the fluid beyond these boundaries. A completely rigorous numerical solution would require a boundary condition for the northward-propagating characteristic at the southern boundary, and one for the southward-propagating characteristic at the northern boundary.

We circumvent these difficulties by employing sponge layers (*e.g.* Israeli and Orszag, 1981) at the edges of the computational domain. These sponge layers absorb outward-propagating

waves whilst minimally affecting the interior. At $y = y_u$ we fix $u = U$, $v = V$, $h = H$, and at $y = y_d$ we artificially fix $u = v = 0$, $h = h_0$, as the actual behaviour of the current beyond the northern boundary is unknown. At the southern boundary the first S gridpoints $y_1, \ldots, y_S$ form the sponge layer. After each time step the values of u_m, v_m and h_m in the sponge layer are multiplied by a sponge coefficient s_m to relax them towards the boundary values, U, V and H. We choose s_m such that the cumulative relaxation factor after one sponge time scale T_s varies linearly from 0 to 1 across the layer,

$$s_m = \left(\frac{m-1}{S-1}\right)^{\Delta t/T_s}, \tag{A.1}$$

where Δt is the length of a time step. An analogous process takes place at the northern boundary, with u_m and v_m relaxed towards 0, and h_m relaxed towards h_0. A drawback of using sponge layers is that the solution will not exactly correspond to the prescribed upstream boundary conditions, which are not rigidly enforced by the sponge layers.

Appendix B. Numerical scheme employed in §6

We obtain our numerical solutions using the centred scheme of Kurganov and Tadmor (2000). This scheme is total variation diminishing for scalar conservation laws, so we multiply (44a) and (44b) by h and use (44c) to rewrite them as conservation laws for the momenta,

$$\frac{\partial}{\partial t}\left(hu + \delta h^2\right) + \frac{\partial}{\partial y}\left(huv + \delta h^2 v\right) = \tfrac{1}{2} yhv, \tag{B.1a}$$

$$\frac{\partial}{\partial t}(hv) + \frac{\partial}{\partial y}\left(hv^2 + \tfrac{1}{2}h^2 - \delta h^2 u\right) = -\tfrac{1}{2} yhu. \tag{B.1b}$$

Equation (44c) is already in conservation form. The traditional components of the Coriolis force appear as nonlinear source terms on the right hand sides of (B.1a) and (B.1b). The y-dependence of f means that y-momentum is not conserved, as fluid moving in the y-direction is subject to a latitudinally varying acceleration by the Coriolis force. The x-momentum is conserved because f is independent of x, so (B.1a) may rewritten as an exact conservation law, but this makes little difference to the computed solution. The Kurganov and Tadmor (2000) scheme is a semi-discrete one, formulated as a system of ordinary differential equations (ODEs) for the evolution of cell-averaged quantities. The spatial discretisation is used to construct discrete fluxes across cell boundaries. The algebraic terms may be easily included alongside the numerical fluxes in the ODE system. No operator splitting is necessary, as would be the case for a Godunov method.

We discretise the domain $y \in [-20, 20]$ using an evenly-spaced grid of N points. The spatial discretisation of Kurganov and Tadmor (2000) uses a 5-point stencil, so we introduce two additional 'ghost' points beyond each boundary of the domain to impose zero-gradient boundary conditions. We integrate forward in time using the second order total variation diminishing Runge–Kutta scheme of Shu and Osher (1989). The integration is numerically stable as long as the ratio of the grid spacing Δy to the time step Δt exceeds the maximum local wave speed $\lambda_{\max}$ at every grid point. This is calculated from the fluxes in (B.1a)–(B.1b) and (44c). At each time step we make Δt as large as possible whilst satisfying $\Delta t \le 0.9\Delta y/\lambda_{\max}$ at all grid points.

Acknowledgement

A.L.S. is supported by an EPSRC Doctoral Training Account award. P.J.D.'s research is supported by an EPSRC Advanced Research Fellowship, grant number EP/E054625/1.

Amante, C., Eakins, B. W., 2009. ETOPO1 1 Arc-Minute Global Relief Model: Procedures, Data Sources and Analysis, NOAA Technical Memorandum NESDIS NGDC-24. Tech. rep., NOAA.

Bretherton, F. P., 1964. Low frequency oscillations trapped near the equator. Tellus 16, 181–185.

Choboter, P. F., Swaters, G. E., 2000. Modeling equator-crossing currents on the ocean bottom. Canadian Applied Mathematics Quarterly 8, 367–385.

Choboter, P. F., Swaters, G. E., 2004. Shallow water modeling of Antarctic Bottom Water crossing the equator. Journal of Geophysical Research – Oceans 109, C03038.

Colin de Verdière, A., Schopp, R., 1994. Flows in a rotating spherical shell: the equatorial case. Journal of Fluid Mechanics 276, 233–260.

Dellar, P. J., 2011. Variations on a beta-plane: derivation of non-traditional beta-plane equations from Hamilton's principle on a sphere. Journal of Fluid Mechanics 674, 174–195.

Dellar, P. J., Salmon, R., 2005. Shallow water equations with complete Coriolis force. Physics of Fluids 17, 106601.

Eckart, C., 1960. Hydrodynamics of Oceans and Atmospheres. Pergamon, Oxford.

Edwards, C. A., Pedlosky, J., 1998. Dynamics of nonlinear cross-equatorial flow. Part I: Potential vorticity transformation. Journal of Physical Oceanography 28, 2382–2406.

Firing, E., 1987. Deep zonal currents in the central equatorial Pacific. Journal of Marine Research 45, 791–812.

Friedrichs, M., Hall, M., 1993. Deep circulation in the tropical North Atlantic. Journal of Marine Research 51 (4), 697–736.

Gerkema, T., Zimmerman, J. T. F., Maas, L. R. M., van Haren, H., 2008. Geophysical and astrophysical fluid dynamics beyond the traditional approximation. Reviews of Geophysics 46, RG2004.

Green, A. E., Naghdi, P. M., 1976. A derivation of equations for wave propagation in water of variable depth. Journal of Fluid Mechanics 78, 237–246.

Grimshaw, R., 1975. A note on the beta-plane approximation. Tellus 27, 351–357.

Hall, M. M., McCartney, M., Whitehead, J. A., 1997. Antarctic Bottom Water Flux in the Equatorial Western Atlantic. Journal of Physical Oceanography 27, 1903–1926.

Hall, M. M., Whitehead, J. A., McCartney, M. S., 1994. Moored measurements of Antarctic Bottom Water at the equator. International WOCE Newsletter 17, 5–8.

Hua, B. L., Moore, D. W., Gentil, S. L., 1997. Inertial nonlinear equilibration of equatorial flows. Journal of Fluid Mechanics 331, 345–371.

Israeli, M., Orszag, S. A., 1981. Approximation of radiation boundary conditions. Journal of Computational Physics 41, 115–135.

Killworth, P. D., 1991. Cross-equatorial geostrophic adjustment. Journal of Physical Oceanography 21, 1581–1601.

Kurganov, A., Tadmor, E., 2000. New high-resolution central schemes for nonlinear conservation laws and convection-diffusion equations. Journal of Computational Physics 160, 241–282.

Leibovich, S., Lele, S., 1985. The influence of the horizontal component of Earth's angular velocity on the instability of the Ekman layer. Journal of Fluid Mechanics 150, 41–87.

Marshall, J., Hill, C., Perelman, L., Adcroft, A., 1997. Hydrostatic, quasi-hydrostatic, and nonhydrostatic ocean modeling. Journal of Geophysical Research 102 (C3), 5733–5752.

Miles, J., Salmon, R., 1985. Weakly dispersive nonlinear gravity waves. Journal of Fluid Mechanics 157, 519–531.

Müller, P., 1995. Ertel's potential vorticity theorem in physical oceanography. Reviews of Geophysics 33, 67–97.

Nof, D., 1990. Why are some boundary currents blocked by the equator? Deep-Sea Research 37, 853–873.
Nof, D., Borisov, S., 1998. Inter-hemispheric oceanic exchange. Quarterly Journal of the Royal Meteorological Society 124, 2829–2866.
Nof, D., Olson, D., Feb. 1993. How do western abyssal currents cross the equator? Deep Sea Research Part I: Oceanographic Research 40, 235–255.
Pedlosky, J., 1987. Geophysical Fluid Dynamics. Springer-Verlag.
Phillips, N. A., 1973. Principles of large scale numerical weather prediction. In: Morel, P. (Ed.), Dynamic meteorology: Lectures delivered at the Summer School of Space Physics of the Centre National d'Études Spatiales. D. Reidel Pub. Co., Dordrecht, Boston, pp. 3–96.
Raymond, W. H., 2000. Equatorial meridional flows: Rotationally induced circulations. Pure and Applied Geophysics 157, 1767–1779.
Rhein, M., Stramma, L., Krahmann, G., 1998. The spreading of Antarctic bottom water in the tropical Atlantic. Deep Sea Research-Part I-Oceanographic Research Papers 45 (4), 507–528.
Ripa, P., 1981. Symmetries and conservation laws for internal gravity waves. In: West, B. J. (Ed.), Nonlinear Properties of Internal Waves. Vol. 76 of AIP Conference Proceedings. American Institute of Physics, New York, pp. 281–306.
Ripa, P., 1982. Nonlinear wave-wave interactions in a one-layer reduced-gravity model on the equatorial β plane. Journal of Physical Oceanography 12, 97–111.
Ripa, P., 1997. "Inertial" oscillations and the β-plane approximation(s). Journal of Physical Oceanography 27, 633–647.
Salmon, R., 1982. Hamilton's principle and Ertel's theorem. In: Tabor, M., Treve, Y. M. (Eds.), Mathematical Methods in Hydrodynamics and Integrability of Dynamical Systems. Vol. 88 of AIP Conference Proceedings. American Institute of Physics, New York, pp. 127–135.
Salmon, R., 2002. Numerical solution of the two-layer shallow water equations with bottom topography. Journal of Marine Research 60, 605–638.
Schopp, R., Colin de Verdière, A., 1997. Taylor columns between concentric spheres. Geophysical & Astrophysical Fluid Dynamics 86, 43–73.
Shchepetkin, A. F., O'Brien, J. J., 1996. A physically consistent formulation of lateral friction in shallow-water equation ocean models. Monthly Weather Review 124, 1285–1300.
Shu, C. W., Osher, S., 1989. Efficient implementation of essentially non-oscillatory shock-capturing schemes, II. Journal of Computational Physics 83, 32–78.
Stephens, J. C., Marshall, D. P., 2000. Dynamical pathways of Antarctic Bottom Water in the Atlantic. Journal of Physical Oceanography 30, 622–640.
Stern, M. E., 1963. Trapping of low frequency oscillations in an equatorial "boundary layer". Tellus 15, 246–250.
Stewart, A. L., Dellar, P. J., 2010. Multilayer shallow water equations with complete Coriolis force. Part 1. Derivation on a non-traditional beta-plane. Journal of Fluid Mechanics, 387–413.
Stommel, H., Arons, A. B., 1960. On the abyssal circulation of the world ocean — 1. Stationary planetary flow patterns on a sphere. Deep-Sea Research 6, 140–154.
Veronis, G., 1963. On the approximations involved in transforming the equations of motion from a spherical surface to the β-plane. I. Barotropic systems. J. Marine Research 21, 110–124.
Veronis, G., 1981. Dynamics of large-scale ocean circulation. In: Warren, B. A., Wunsch, C. (Eds.), Evolution of Physical Oceanography. Massachusetts Institute of Technology Press, pp. 140–183.
White, A. A., 2002. A view of the equations of meteorological dynamics and various approximations. In: Norbury, J., Roulstone, I. (Eds.), Large-Scale Atmosphere-Ocean Dynamics 1: Analytical Methods and Numerical Models. Cambridge University Press, Cambridge, pp. 1–100.
White, A. A., Bromley, R. A., 1995. Dynamically consistent, quasi-hydrostatic equations for global models with a complete representation of the Coriolis force. Quart. J. Roy. Meteorol. Soc. 121, 399–418.
Whitham, G. B., 1974. Linear and Nonlinear Waves. Wiley New York.